

1 **A flexible three-dimensional stratocumulus, cumulus and**
2 **cirrus cloud generator (3DCLOUD) based on drastically**
3 **simplified atmospheric equations and the Fourier**
4 **transform framework.**

5
6 **F. Szczap¹, Y. Gour^{1,4}, T. Fauchez², C. Cornet², T. Faure³, O. Jourdan¹, G.**
7 **Penide² and P. Dubuisson²**

8 [1]{Laboratoire de Météorologie Physique, UMR 6016, CNRS, Aubière, France}

9 [2]{Laboratoire d'Optique Atmosphérique, UMR 8518, CNRS, Villeneuve d'Ascq, France}

10 [3]{Laboratoire d'Ingénierie pour les Systèmes Complexes, Clermont-Ferrand, France}

11 [4]{Laboratoire de Météorologie Physique, Institut Universitaire de Technologie d'Allier,
12 Montluçon, France}

13
14 Correspondence to: F. Szczap (szczap@opgc.univ-bpclermont.fr)

15
16 **Abstract**

17 The 3DCLOUD algorithm for generating stochastic three-dimensional (3D) cloud fields is
18 described in this paper. The generated outputs are 3D optical depth (τ) for stratocumulus and
19 cumulus fields and 3D ice water content (IWC) for cirrus clouds. This model is designed to
20 generate cloud fields that share some statistical properties observed in real clouds such as the
21 inhomogeneity parameter ρ (standard deviation normalized by the mean of the studied
22 quantity), the Fourier spectral slope β close to $-5/3$ between the smallest scale of the
23 simulation to the outer L_{out} (where the spectrum becomes flat). Firstly, 3DCLOUD
24 assimilates meteorological profiles (humidity, pressure, temperature and wind velocity). The
25 cloud coverage C , defined by the user, can also be assimilated, but only for stratocumulus
26 and cumulus regime. 3DCLOUD solves drastically simplified basic atmospheric equations, in
27 order to simulate 3D cloud structures of liquid or ice water content. Secondly, the Fourier

1 filtering method is used to constrain the intensity of ρ , β , L_{out} and the mean of τ or IWC
2 of these 3D cloud structures. 3DCLOUD model was developed to run on a personal computer
3 under Matlab environment with the Matlab statistics toolbox. It is used to study 3D
4 interactions between cloudy atmosphere and radiation.

5

6 **1 Introduction**

7

8 Clouds have a significant effect on the Earth radiation budget. They reflect the solar radiation
9 and reduce the warming of the Earth (albedo effect). They also create a greenhouse effect by
10 trapping the thermal radiation emitted from the Earth's surface, reducing the radiative cooling
11 of the Earth (Collins and Satoh, 2009). Cloud feedback has remained, however, the largest
12 uncertainty in the study of climate sensitivity for almost twenty years (Bony et al., 2006). In
13 almost all climate models, clouds are assumed plane-parallel with homogeneous optical
14 properties (PPH), and radiation codes use a one-dimensional (1D) scheme. Therefore,
15 improving parameterisations of clouds in large-scale model, especially their interaction with
16 radiation, is a challenge in order to reduce uncertainty in model projections of the future
17 climate (Illingworth and Bony, 2009). Improved global characterization of the three
18 dimensional (3D) spatial distribution of clouds is, thus, necessary (Clothiaux et al., 2004).

19 Moreover, satellite passive sensors, such as multi-spectral and multi-angular radiometers, and
20 satellite active sensor, such as LIDAR and RADAR in the A-train mission, allow the retrieval
21 of cloud horizontal and vertical optical properties with an adequate spatial and temporal
22 coverage. For practical and computational cost purposes, interpretation of such measurements
23 generally also assumes 1D radiative algorithm and PPH cloud. This assumption can be far
24 from being realistic and leads to biases on the retrieved properties from passive sensors
25 (Barker and Liu, 1995; Várnai and Marshak, 2002; Lafont and Guillemet, 2004; Cornet et al.,
26 2005; Várnai and Marshak, 2007; Cornet et al., 2013) and active sensors (Battaglia and
27 Tanelli, 2011). These biases depend at least, on the cloud coverage and on the variability of
28 cloud optical depth or water content. This variability is quantified by an inhomogeneity
29 parameter, often defined as the standard deviation normalized by the mean of the studied
30 quantity (Szczap et al., 2000; Carlin et al., 2002; Oreopoulos and Cahalan, 2005; Sassen et al.,
31 2007; Hill et al., 2012).

1 Determining the significance of the 3D inhomogeneity of clouds for climate and remote
2 sensing applications requires the measurement and the simulation of the full range of actual
3 cloud structure. Apart from the computational time, accurate 3D cloudy radiative transfer
4 problem is not an issue, per se (Evans and Wiscombe, 2004). Monte Carlo transfer models
5 can indeed accurately and efficiently compute radiative properties for arbitrary cloud fields
6 (Battaglia and Mantovani, 2005; Pincus and Evans, 2009; Mayer, 2009; Cornet et al., 2010;
7 Battaglia and Tanelli, 2011; Cornet et al., 2013; Fauchez et al., 2013). The difficulty is to
8 generate cloud property fields that are statistically representative of cloud fields in nature.

9 Cloud fields generated by dynamic cloud models, such as the cloud resolving model (CRM)
10 or the large-eddy simulation model (LES), are very attractive, as they contain the state of the
11 art of physical processes (resolution of atmospheric equations, detailed microphysics,
12 radiation, .etc.). The goal of the LES approach is to simulate the three-dimensional
13 atmospheric turbulent flows. There are different scales of turbulent eddies; large eddies (from
14 100 to 1000 m and more) that are produced directly by the instability of the mean flow and
15 small eddies (from a few centimeters to 100 m) as well as by the energy-cascade process from
16 the larger eddies (Moeng, 1984). LES seeks to capture accurately the larger eddies, while only
17 modeling the smaller ones. Instead of reproducing all the scales of turbulence flow, they can
18 integrate a flow in which small scale details are removed from the solution. The spatial
19 filtered equations can, therefore, be integrated with available resources (Bryan et al., 2003).
20 Nevertheless, they are still very expensive to run in a 3D domain.

21 Stochastic models have the capability to simulate quickly realistic 2D and 3D cloud structures
22 with just a few parameters. Examples of these types of cloud models are: the bounded cascade
23 model (Cahalan et al., 1994 ; Marshak et al., 1998), the IAAFT algorithm (Venema et al.,
24 2006), the SITCOM model (Di Giuseppe and Thompkins, 2003), the tdMAP model (Benassi
25 et al., 2004), the model developed by Evans and Wiscombe (2004) for low liquid clouds
26 (stratocumulus and cumulus) or by Alexandrov et al. (2010) and the Cloudgen model (Hogan
27 and Kew, 2005) for high ice clouds (cirrus). These stochastic models are based on fractal or
28 Fourier framework. The scale invariant properties observed in real clouds can be controlled.
29 The power spectra of the logarithm of their optical properties (optical depth, liquid water
30 content or liquid water path for low clouds and ice water content for high clouds) typically
31 exhibits a spectral slope of around $-5/3$ (Davis et al., 1994 ; Cahalan et al., 1994 ; Davis et al.,
32 1996 ; Davis et al., 1999 ; Davis et al., 1997 ; Benassi et al., 2004 ; Hogan and Kew, 2005 ;

1 Hill et al., 2012, Fauchez et al., 2014) from small scale (a few meters) to the "integral scale"
2 or the outer scale (few tenth to hundred kilometres), where the spectrum becomes flat (i.e.
3 decorrelation occurs). The disadvantage of such models arises from the fact that effects of
4 meteorological processes are not always considered and dominant scales of organization
5 related to turbulent eddy due, for example, to wind shear, convection, and entrainment are not
6 directly modeled. At the same time, it should be noted that Cloudgen does consider the effect
7 of wind shear on cirrus cloud.

8 The aim of the 3DCLOUD algorithm is to reconcile these two approaches. In Sect. 2, we
9 describe the 3DCLOUD generator. In Sect 3, 3DCLOUD outputs are compared to LES
10 outputs to check the validity of the chosen basic atmospheric equations. In Sect 4,
11 stratocumulus, cumulus and cirrus examples provided by 3DCLOUD are presented.

12

13 **2 The 3DCloud generator**

14

15 3DCLOUD generates, in two distinct steps (see Fig. 1), a 3D optical depth field for
16 stratocumulus and cumulus or a 3D ice water content field for cirrus clouds. These cloud
17 fields were chosen as most of the papers dealing with scale invariant properties focus on
18 liquid water path and optical depth for stratocumulus and cumulus and on ice water content
19 for cirrus. During the first step, meteorological vertical profiles (temperature, pressure, wind,
20 humidity), defined by the user, are assimilated and basic atmospheric equations are resolved.
21 During the second step, cloud scale invariant properties are constrained in a Fourier
22 framework. At the same time, a gamma distribution of local optical depth or IWC is mapped
23 onto the LWC/IWC generated during the first step. This gamma distribution is iteratively
24 computed in such way that the mean optical depth or IWC and the inhomogeneity parameter
25 satisfy the values imposed by the user. Details of these two steps are presented below.

26 **2.1 Step 1: the 3D LWC/IWC generator**

27 The essential basic quantities to generate cloud fields are the condensed water mixing ratio
28 $q_c = q_l + q_i$ where q_l is the liquid water mixing ratio and q_i is the ice water mixing ratio, the
29 wind velocity vector \mathbf{u} , air pressure p , temperature T , and vapour water mixing ratio q_v .

1 Mixing ratios are the mass of vapour or condensed water per unit of dry air mass. We describe
 2 in this section, the equations used to generate clouds with the associated simplifications used.

3 **2.1.1 The simplification of basic atmospheric equations**

4 The continuity and momentum equations of the atmosphere can be written (Houze, 1993):

$$5 \left\{ \begin{array}{l} \frac{D\rho}{Dt} = -\rho \nabla \cdot \mathbf{u} \\ \frac{D\mathbf{u}}{Dt} = -\frac{1}{\rho} \nabla p - f\mathbf{k} \wedge \mathbf{u} - g\mathbf{k} + \mathbf{F} \end{array} \right. \quad (1)$$

6 where t is time, ρ the air density, f the Coriolis parameter, g the acceleration due to
 7 gravity and \mathbf{F} the acceleration due to other forces (frictional acceleration for example).
 8 $D/Dt = \partial/\partial t + \mathbf{u} \cdot \nabla$ is the Lagrangian derivative operator following a parcel of air, $\partial/\partial t$ is the
 9 Eulerian derivative operator and ∇ is the three-dimensional gradient operator. $\mathbf{u} = u\mathbf{i} + v\mathbf{j} +$
 10 $w\mathbf{k}$ is the wind velocity vector with horizontal components u , v and vertical component w
 11 projected in the Cartesian geometry system, where \mathbf{i} , \mathbf{j} and \mathbf{k} are the unit vectors in the x , y
 12 and z directions. The continuity and momentum equations of the atmosphere under the
 13 anelastic and Boussinesq approximation, assuming shallow motion, neglecting Coriolis
 14 parameter, neglecting frictional forces, and neglecting the molecular viscosity can be written
 15 (Holton, 2004, p. 117 ; Houze, 1993, p. 35 ; Emanuel, 1994, p. 11)

$$16 \left\{ \begin{array}{l} \nabla \cdot \mathbf{u} = 0 \\ \frac{D\mathbf{u}}{Dt} = -\frac{1}{\rho_0} \nabla p^* + B\mathbf{k} \end{array} \right. \quad (2)$$

17 where B is the buoyancy acceleration, ρ_0 is the constant mean value of air density and p^* is
 18 the pressure perturbations. The above differential operators are valid only in the limit when
 19 δt , δx , δy and δz approach 0 (Pielke, 2002, p. 41). Nevertheless, turbulent motions (shear
 20 induced eddies, convection eddies) have spatial and temporal variations at scales much
 21 smaller than those resolved by LES and 3DCLOUD. If we assume field variables can be
 22 separated in slowly varying mean field and rapidly varying turbulent component, and if we
 23 apply the Reynolds decomposition, we can rewrite the above equation set as:

$$24 \left\{ \begin{array}{l} \nabla \cdot \mathbf{u} = 0 \\ \frac{D\mathbf{u}}{Dt} = -\frac{1}{\rho_0} \nabla p^* + B\mathbf{k} + \Phi \end{array} \right. \quad (3)$$

1 where Φ is the three dimensional convergence of the eddy flux of moment (Houze, 1993, p.
 2 42), the turbulent flux (Holton, 2002, p 119) or the sub-grid correlation term (Pielke, 2002, p.
 3 44). The Reynolds decomposition is not used in LES. The atmospheric equations are derived
 4 by spatial filtering, where a special function is applied. Thus, the filtering operation acts on
 5 atmospheric quantities and separates them in two categories: the resolved one (large eddy)
 6 and unresolved one (subgrid-scale). An unknown term remains in the filtered equations of
 7 LES, often called the subgrid-scale stress, which needs to be parameterized or estimated with
 8 the help of subgrid-scale modeling. This subgrid-scale stress for LES equations is analogous
 9 to the Φ term for Reynolds decomposition. In 3DCLOUD, the Φ term is voluntarily
 10 neglected. Indeed, the guiding idea of 3DCLOUD is to simulate, in the fastest way, 3D
 11 fluctuations of LWC/IWC of a cloud showing turbulent properties (or invariant scale
 12 properties).

13 When water phase changes are only associated with condensation and evaporation (or
 14 sublimation), the first law of thermodynamics can be written (Houze, 93):

$$15 \quad \frac{D\theta}{Dt} = -\frac{L}{C_p \Pi} \frac{Dq_v}{Dt} \quad (4)$$

16 where $L = 2500 \text{ kJkg}^{-1}$ and $L = 2800 \text{ kJkg}^{-1}$ are the usual latent heat of vaporization of water
 17 and ice, respectively. $C_p = 1.004 \text{ kJkg}^{-1}\text{K}^{-1}$ is the usual specific heat of dry air at constant
 18 pressure, θ is the potential temperature and $\Pi = (p/p_0)^\kappa = T/\theta$ is the Exner function where
 19 $p_0 = 1000 \text{ hPa}$ and $\kappa = 0.286$. In addition to the equation of motion and the first law of
 20 thermodynamics, air parcels follow the water continuity equation:

$$21 \quad \frac{Dq_i}{Dt} = S_i, \quad i = 1, \dots, n \quad (5)$$

22 where S_i are the sum of the sources and sinks for a particular category (among n categories)
 23 of water indicated by i (vapor, solid, liquid water category for example).

24 As the horizontal extension of the simulated cloud fields is around a few km, horizontal
 25 pressure is assumed to be constant. Therefore, the current version of 3DCLOUD does not
 26 have a large enough domain to contain power in the mesoscale. All these considerations lead
 27 to a dramatic simplification of the dynamic equations. The simplified equations of
 28 3DCLOUD governing the formation of 3D cloud structures are:

$$\begin{cases}
\frac{D\mathbf{u}}{Dt} = g \left(\frac{\theta_v^*}{\theta_{v0}} - q_c \right) \mathbf{k} - \frac{1}{\rho_0} \frac{\partial p^*}{\partial z} \mathbf{k} \\
\nabla \cdot \mathbf{u} = 0 \\
\frac{D\theta}{Dt} = \frac{L}{C_p \Pi} \xi \\
\frac{Dq_v}{Dt} = -\xi \\
\frac{Dq_c}{Dt} = \xi
\end{cases} \quad (6)$$

2 where the reference state is denoted by subscript $_0$ and the deviation from the reference state
3 by an asterisk, $\theta_v = \theta(1 + 0.61q_v)$ is the virtual potential temperature. For stratocumulus and
4 cumulus fields ξ is estimated as:

$$5 \quad \xi = \min(q_{vs} - q_v, q_c) \Delta t \quad (7)$$

6 where Δt is the simulation time step and $q_{vs}(T, p)$ is the saturation mixing ratio derived
7 from Thetens and Magnus formula: $q_{vs}(T, p) = \frac{0.622P_{sat}}{(p/100 - 0.378P_{sat})}$, where

$$8 \quad P_{sat} = 6.107 \exp \left[\frac{4028(T - 273.15)}{234.82(T - 38.33)} \right] \quad \text{for water,} \quad P_{sat} = 6.107 \times 10^{\left[\frac{9.5(T - 273.15)}{265.5 + (T - 273.15)} \right]} \quad \text{for ice.}$$

9 Computation of ξ at each simulation step is based on the work of Asai (1965). For cirrus
10 clouds, condensation, evaporation and ice crystals sedimentation processes are very complex
11 and still not well understood (Karcher and Spichtinger, 2009). In order to take into account
12 super-saturation and sub-saturation regions in cirrus clouds in a very simple way, we used the
13 parameterisation of Starr and Cox (1985) to compute the values of ξ every 2.5 min.
14 Sedimentation processes are taken into account in Eq. (5.5) by adding ice fall speed v_{fall}
15 taken from Starr and Cox (1985):

$$16 \quad v_{fall} = \frac{1.5}{6} \log_{10} \left[\max(IWC, 1 \times 10^{-6}) \right] + 1.5 \quad (8)$$

17 where v_{fall} is in m/s and the ice water content IWC in g/m^3 .

18

1 2.1.2 Assimilation of meteorological profiles and cloud coverage

2 In order to control the structure and nature of clouds and especially vertical position and
 3 extension, it is necessary to impose a large-scale environment. Practically, forcing terms are
 4 added to the 3DCLOUD equations to nudge the solutions towards observations. Our state
 5 observations are the initial meteorological profiles (provided by the user for example) and do
 6 not change during the simulation. The technique used is based on the initialization integration
 7 method (Pielke, 2002). Consequently, 3DCLOUD equations become:

$$\begin{cases}
 \frac{Du}{Dt} = G_u(z) [u_{ini}(z) - \bar{u}(z)] \\
 \frac{Dv}{Dt} = G_v(z) [v_{ini}(z) - \bar{v}(z)] \\
 \frac{Dw}{Dt} = g \left(\frac{\theta_v^*}{\theta_{v0}} - q_c \right) - \frac{1}{\rho_0} \frac{\partial p^*}{\partial z} \\
 \nabla \cdot \mathbf{u} = 0 \\
 \frac{D\theta}{Dt} = \frac{L}{C_p \Pi} \xi + G_\theta(z) [\theta_{ini}(z) - \theta] \\
 \frac{Dq_v}{Dt} = -\xi + G_{q_v}(z) [q_{vini}(z) - q_v] \\
 \frac{Dq_c}{Dt} = \xi
 \end{cases} \quad (9)$$

10 where for variables X , $\bar{X}(z)$ is the mean of X at height z and quantities $G_X(z)$ are
 11 adjusted during the simulation in such a way that X or $\bar{X}(z)$ do not diverge far from the
 12 initial conditions $X_{ini}(z)$. In a general way, G is the inverse of timescale but, because the
 13 contribution of G is artificial, it must not be a dominant term in the governing equations and
 14 should be scaled by the slowest physical adjustment processes in the model (Cheng et al.,
 15 2001). This timescale was first set to 1h but this value was found to be too large and must be
 16 adjusted as a function of altitude, especially at height where large vertical gradients of X
 17 appear (e.g., at the top of a stratocumulus cloud, for example). Therefore, we developed a
 18 very fast and simple numerical method to adjust the values of $G_X(z)$ during the simulation.

19 At each level, we compute the relative difference $\alpha_X(z) = \frac{X_{ini}(z) - \bar{X}(z)}{\bar{X}(z)} \cdot 100$. $G_X(z)$ is

1 assumed to be proportional to $\alpha_X(z)$ and is estimated as

$$2 \quad G_X(z) = \min \left[G_{\min} + \frac{G_{\max} - G_{\min}}{\alpha_{X,\max}} \alpha_X(z), G_{\max} \right] \quad \text{where} \quad G_{\min} = \frac{1}{3600} \text{ s}^{-1} \quad \text{and} \quad G_{\max} = \frac{1}{2\Delta t}.$$

3 Values of $\alpha_{X,\max}$ were estimated during our numerous numerical experiments. For
 4 stratocumulus and cumulus, $\alpha_{X,\max}$ values for horizontal wind, temperature and humidity are
 5 20%, 2% and 20% respectively and for cirrus, $\alpha_{X,\max}$ values are 20%, 10% and 10%,
 6 respectively.

7 The cloud coverage C is defined as the fraction of the number of cloudy pixels to the total
 8 number of pixels in the 2D horizontal plan. The value of C is chosen with the assimilation of
 9 initial meteorological profiles. At each time step, the initial profile of vapour mixing ratio
 10 $q_{v_{ini}}(z)$ is modified between cloud base and top height if $C \geq 50\%$ or between ground and
 11 cloud top height if $C < 50\%$ until C agrees with the desired value within few percents. The
 12 new "initial" profile of vapour mixing ratio $q_{v_{ini}}^{new}(z)$ is computed from the currently simulated

$$13 \quad (\text{old}) \text{ profile of vapour mixing ratio } q_{v_{ini}}^{old}(z) \text{ as } q_{v_{ini}}^{new}(z) = q_{v_{ini}}^{old}(z) \pm \frac{n_z - n_{base}}{n_{top} - n_{base}} q_{v_{ini}}^{old}(z) \times \frac{0.1}{100}$$

14 where z is height, and n_z , n_{top} and n_{base} are the levels indexes (in z direction) corresponding
 15 to cloud top height and to cloud base height (or ground), respectively.

16 This method gives satisfactory results for stratocumulus and cumulus cloud fields (see Sect.
 17 4.1.2), but not for cirrus fields. This is because condensation/evaporation and dynamic
 18 processes are different for stratocumulus/cumulus and cirrus regimes. Indeed, for liquid and
 19 warm stratocumulus/cumulus regime, liquid super or sub-saturation regions are not allowed in
 20 3DCLOUD. Therefore, the distinction between cloudy and free cloud voxels is sharp.
 21 Moreover, as stratocumulus/cumulus fields are often driven by convection processes in a
 22 well-mixed planetary boundary layer, vertical correlation occurs between cloudy voxels (free
 23 cloud voxels) and updrafts (downdrafts). Thus, the fractional cloud coverage is easily
 24 controlled by adjusting the vertical profile of vapor mixing ratio during the simulation. By
 25 contrast, in ice cirrus regimes, (large) ice crystals can survive even if ice relative humidity is
 26 less than 100%. Ice super or sub-saturation regions are often observed in cirrus and are taken
 27 into account in the Starr and Cox parameterization used in 3DCLOUD. Therefore, many
 28 cloudy voxels still exist in our cirrus simulations, even if the ice water content is very small.

1 The distinction between cloudy and free cloud voxels is, thus, very tenuous. Moreover, cirrus
 2 dynamics is often driven by wind shear: small fractional cloud coverage can exist at the top of
 3 the cirrus field due to convection or radiative cooling coexisting with large fractional cloud
 4 coverage and can also exist at the bottom of cirrus field due to wind shear. Finally, the total
 5 cloud coverage could be large. If we adjust the vertical profile of vapor mixing ratio during
 6 the simulation in the same way as for the stratocumulus/cumulus field, the total cloud
 7 coverage will be difficult to control. Further investigations are thus needed to perfectly
 8 control the cloud coverage of cirrus simulated by 3DCLOUD.

9

10 **2.1.3 Implementation of 3DCLOUD algorithm**

11 To implement the previously described equations, space is divided in
 12 $(N_x + 2) \times (N_y + 2) \times (N_z + 2)$ cells or voxels where N_x , N_y and N_z are the voxel numbers in
 13 each direction. A voxel is characterized by its spatial resolution with $\Delta x = \Delta y \neq \Delta z$.
 14 Horizontal extensions are $L_x = L_y$ and can be different from the vertical extension L_z . In
 15 order to take into account the boundary conditions, one layer of voxel is added around the
 16 simulation domain.

17 A semi-Lagrangian scheme was chosen to solve the equation:

$$18 \quad \frac{DX}{Dt} = \frac{\partial X}{\partial t} + \mathbf{u} \cdot \nabla X = 0 \quad (10)$$

19 where X is a scalar advected by the wind velocity \mathbf{u} . X can be the potential temperature θ ,
 20 the condensed water q_c or the vapor mixing ratios q_v , and also the three components of wind
 21 velocity u , v and w . Two steps are needed in order to compute the value of $X(x, t + \Delta t)$ at
 22 a fixed position x and at time $t + \Delta t$. $X(x, t)$ and $\mathbf{u}(x, t)$ are known values and Δt is the
 23 time step. First, we compute the previous position $p(X, t - \Delta t) = x - \mathbf{u}(x, t) \Delta t$ of X at time
 24 $t - \Delta t$. In a second step, we compute the value of $X(p, t)$ at the position p and at the time t
 25 by an interpolation scheme. This interpolated value $X(p, t)$ is the desired value $X(x, t + \Delta t)$.
 26 The main advantage of this approach is that the time step is not restricted by the Courant-
 27 Friedrichs-Lewy stability limit, but by the less restrictive condition that parcels do not

1 overtake each other during the time step (Riddaway, 2001). Therefore, at each iteration, the
 2 maximum value of time step Δt_{\max} can be roughly estimated as
 3 $\Delta t_{\max} = 1 / (\max |\Delta u / \Delta x| + \max |\Delta v / \Delta y| + \max |\Delta w / \Delta z|)$. The accuracy of this approach depends
 4 on the accuracy of the interpolation scheme. Due to CPU time, we chose a linear
 5 interpolation, which, unfortunately, provides numerical dissipations. However, this drawback
 6 is overcome using the Fourier transform performed in the second step of the 3DCLOUD
 7 algorithm (see Section 2.2.2).

8 As the Fourier transform is easy to implement, this method was chosen to solve the equation
 9 $\nabla \cdot \mathbf{u} = 0$. In the Fourier domain, the gradient operator ∇ is equivalent to the multiplication
 10 by $i\mathbf{k}$, where $i \equiv \sqrt{-1}$ and \mathbf{k} is the wave number vector. Thus, the following equation
 11 $i\mathbf{k} \cdot \hat{\mathbf{u}}(\mathbf{k}) = 0$, where $\hat{\mathbf{u}}$ is the transform of wind velocity \mathbf{u} in the Fourier domain, has to be
 12 solved. This implies that the Fourier transform of the velocity of a divergent free field is
 13 always perpendicular to its wave numbers. Therefore, the quantity $1/k^2 (\mathbf{k} \cdot \hat{\mathbf{u}}(\mathbf{k})) \mathbf{k}$ is
 14 removed from $\hat{\mathbf{u}}$. Keeping the real part of inverse transform of $\hat{\mathbf{u}}$ provides the new wind
 15 velocity \mathbf{u} with the desired free divergent property.

16 Lateral periodic conditions and continuity conditions to bottom and top are applied. For wind
 17 velocity, free slip boundary conditions are applied at the bottom and top of the domain, which
 18 are assumed to be a solid wall (i.e. $w = 0$). But, as the Fourier transform (which is needed to
 19 solve the equation $\nabla \cdot \mathbf{u} = 0$) requires periodic conditions, it provides spurious oscillations
 20 during the simulations. In order to limit this effect, extra levels with wind velocity set to zero
 21 are added under and above the model domain.

22 The 3DCLOUD algorithm to simulate 3D structures of LWC or IWC is, in summary:

- 23 1) Definition of initial meteorological profiles u_{ini} , v_{ini} , θ_{ini} , $q_{v_{ini}}$ from idealized cloud
 24 conceptual models or from the user. The vertical pressure profile is generally computed from
 25 the hydrostatic law, but can be provided by the user.
- 26 2) Initial perturbations \mathbf{u}' are added to wind velocity \mathbf{u} . \mathbf{u}' is free-divergent and turbulent
 27 with a spectral slope of -5/3 (see more explanations in Sect. 2.2.2).
- 28 3) Assimilation of initial meteorological profiles (optional, see Eq. 9 and Sect. 2.1.2).
- 29 4) Constrain of divergent-free velocity \mathbf{u} (see Eq. 9).

- 1 5) Computation of ice fall speed v_{fall} (only for cirrus cloud, see Eq. 8).
- 2 6) Advection of u , v , w , θ , q_v and q_c by wind velocity \mathbf{u} (see Eq. 10).
- 3 7) Modification of θ , q_v and q_c due to evaporation/condensation processes (see Eq. 7).
- 4 8) Modification of the vertical velocity due to buoyancy (see Eq. 9).
- 5 9) Modification of $q_{v_{mi}}$ in order to assimilate cloud coverage C (optional, only for
- 6 stratocumulus and cumulus, see Sect. 2.1.2).
- 7 10) Return to 3) until maximum iteration number is reached.
- 8 11) Computation of LWC or IWC.

9

10 **2.2 Step 2 : statistical adjustment**

11 Hereafter, we present the second step of the 3DCLOUD algorithm that is the methodology to
 12 adjust, according to user requirements, the mean optical depth $\bar{\tau}$ (or the mean ice water
 13 content \overline{IWC}) and the inhomogeneity parameter of the optical depth ρ_τ (or the ice water
 14 content ρ_{IWC}) from the LWC (or from the IWC) simulated at the step 1. The distribution of τ
 15 or IWC is assumed to follow a gamma distribution. Indeed, distribution of τ and IWC are
 16 usually well represented by a lognormal or gamma distribution (Cahalan et al., 1994; Barker
 17 et al., 1996; Carlin et al., 2002; Hogan and Illingworth, 2003; Hogan and Kew, 2005). The
 18 scale invariant cloud properties, controlled at each level, are characterised by the spectral
 19 exponent β_{1D} close to -5/3 (slope β of the one dimension wave number spectrum in log-log
 20 axes of the Fourier space). This spectral slope is computed from the outer scale L_{out} (defined
 21 by the user) to the smaller scale (voxel horizontal size).

22

23 **2.2.1 Control of the mean and of the inhomogeneity parameter**

24 The relation between *local* optical depth $\tau(x, y, z)$, liquid water path LWP and density of
 25 water ρ_l in each voxel is given by (Liou, 2002):

$$1 \quad \tau(x, y, z) = \frac{3}{2\rho_l} \frac{\text{LWP}(x, y, z)}{R_{\text{eff}}} \text{ with } \text{LWP}(x, y, z) = \rho_{\text{air}} q_c(x, y, z) \Delta z \quad (11)$$

2 where x, y, z are the spatial positions inside the simulation domain, $\text{LWP}(x, y, z)$ is the
 3 *local* liquid water path and Δz is the vertical resolution. *Local* quantity means that the
 4 quantity is estimated inside a voxel. The optical depth $\tau(x, y)$ for each pixel is the sum of
 5 *local* optical depths along the z-axis:

$$6 \quad \tau(x, y) = \sum_{z=1}^{N_z} \tau(x, y, z). \quad (12)$$

7 The mean optical depth $\bar{\tau}$ is then defined as:

$$8 \quad \bar{\tau} = \frac{1}{N_x N_y} \sum_{x=1}^{N_x} \sum_{y=1}^{N_y} \tau(x, y). \quad (13)$$

9 In the same way, for ice cloud, the mean IWC is obtained with

$$10 \quad \overline{\text{IWC}} = \frac{1}{N_x N_y N_z^*} \sum_{x=1}^{N_x} \sum_{y=1}^{N_y} \sum_{z=1}^{N_z^*} \text{IWC}(x, y, z) \quad (14)$$

11 where N_z^* is the number of layers between cloud top and cloud bottom.

12 To describe the amplitude of the optical depth for 1D and 2D overcast cloud, Szczap et al.
 13 (2000) defined the inhomogeneity parameter of optical depth ρ_τ . For 3D broken fields, this
 14 parameter is defined according to

$$15 \quad \rho_\tau = \frac{\sigma[\tau^{>0}(x, y)]}{\bar{\tau}^{>0}(x, y)} \quad (15)$$

16 where $\sigma[\tau^{>0}(x, y)]$ and $\bar{\tau}^{>0}(x, y)$ are the standard deviation and the mean of the strictly
 17 positive optical depth.

18 Due to the flexibility of the mathematical formulation of the gamma distribution and to its
 19 ability to mimic the attributes of other positive-value distributions, such as lognormal and
 20 exponential distributions, we choose to control $\bar{\tau}$ or $\overline{\text{IWC}}$ and ρ_τ or ρ_{IWC} by mapping
 21 theoretical gamma-distributed properties onto the simulated properties. This mapping
 22 technique is analog to the "amplitude adaptation" technique explained in Venema et al.

1 (2006), where amplitudes are adjusted based on their ranking. The gamma distribution is a
 2 two-parameter family of continuous probability distribution. It has a shape parameter a and
 3 scale parameter b . The equation defining the probability density as a function of a gamma-
 4 distributed random variable Y is:

$$5 \quad Y = f(\mu; a, b) = \frac{1}{b^a \Gamma(a)} \mu^{a-1} e^{-\mu/b} \quad (16)$$

6 where $\Gamma(\cdot)$ is the gamma function. We develop a simple iterative algorithm, where values of
 7 a and b are adjusted until mean and inhomogeneity parameters reach the required user
 8 values within few percents.

9

10 **2.2.2 Control of invariant scale properties by adjustment of spectral exponent** 11 **in Fourier space**

12 The spectral slope value β_{1D} of the horizontally 2D field is adjusted according to the
 13 following methodology. As proposed by Hogan and Kew (2005), we choose to manipulate 2D
 14 plan of Fourier amplitudes of *local* optical depth τ_{2D} (or IWC_{2D}) with a 2D Fourier
 15 transform performed at each height of cloudy layer. Suppose a 2D isotropic field $g(x, y)$
 16 characterized by a Gaussian probability density function (PDF) and a 1D power spectrum
 17 $E_1(k)$ with a spectral slope β_{1D} at all scales defined as:

$$18 \quad E_1(k) = \widehat{E}_1 k^{-\beta_{1D}} \quad (17)$$

19 where k is the wave number in any direction and \widehat{E}_1 is the spectral energy density at $k = 1$
 20 m^{-1} . Following Hogan and Kew (2005), for the idealized case where $g(x, y)$ is continuous at
 21 small scales and infinite in extent, its 2D spectral density matrix $E_2(k_x, k_y)$ can be written as

$$22 \quad E_2(k) = \kappa \widehat{E}_1 k^{-\beta_{1D}-1} \quad (18)$$

23 where $k = \sqrt{k_x^2 + k_y^2}$ and κ a constant. In general, a 2D cloud layer of τ_{2D} (or IWC_{2D}) is
 24 anisotropic and, in our case, the optical depth (or IWC) is gamma-distributed. Therefore, the

1 1D power spectrum $E_1(k)$ seldom has the required spectral slope β_{1D} . In this context, a
 2 numerical method has to be developed to perform our objectives.

3 Let set \widehat{Y}_{2D} be the 2D Fourier transform of Y_{2D} , where Y_{2D} can be τ_{2D} (or IWC_{2D}) at a given
 4 cloudy layer. This quantity, estimated with the help of a direct 2D Fast Fourier Transform
 5 algorithm can be written as:

$$6 \quad \widehat{Y}_{2D}(k) = E_{2D}(k) \exp(i\varphi_{2D}(k)) \quad (19)$$

7 where $E_{2D} = |\widehat{Y}_{2D}|$ is the magnitude or spectral energy, $\varphi_{2D}(k)$ are the phase angles and
 8 $k = \sqrt{k_x^2 + k_y^2}$ is the absolute wave number. The cloud field domain is defined to measure L_x
 9 and L_y and they have spatial resolutions of Δx and Δy . The resulting wave number for E_{2D}
 10 ranges from $-K_x$ to $+K_x$ with a resolution of $\Delta k_x = 1/L_x$, where $K_x = 1/2\Delta x$. It is similar for
 11 k_y direction.

12 Our objective is to modify spectral energy $E_{2D}(k)$ in such a way that the 1D spectral slope
 13 value μ_{1D} estimated in one dimension from Y_{2D} for $k \geq k_{out}$ ($k_{out} = 1/L_{out}$) satisfies the
 14 desired value β_{1D} required by the user. Practically, μ_{1D} is defined as:

$$15 \quad \mu_{1D} = (\beta_x + \beta_y) / 2 \quad (20)$$

16 where β_x and β_y are the 1D spectral slope values of \widehat{Y}_{2D} estimated in the x and y directions
 17 respectively.

18 In order to conserve the spatial repartition of Y_{2D} , we keep $\varphi_{2D}(k)$ phase angles unchanged
 19 for all values of k . We also keep unchanged $E_{2D}(k)$ for $k < k_{out}$. For $k \geq k_{out}$, two 2D matrix
 20 $E_{2D}^*(k)$ and $E_{2D}^{**}(k)$ can be computed. $E_{2D}^*(k)$ is based on Eq. (18) and is defined as:

$$21 \quad E_{2D}^*(k) = \frac{k^{(-\beta_{1D}-1)}}{k_{out}^{(-\beta_{1D}-1)}} E_{2D}(k = k_{out}) \quad (21)$$

22 whereas $E_{2D}^{**}(k)$ is defined as:

$$E_{2D}^{**}(k) = \frac{E_{2D}(k)}{E_{2D}(k) k_{out}^{(-\beta_{1D}-1)}} k^{(-\beta_{1D}-1)} \overline{E_{2D}}(k = k_{out}) \quad (22)$$

where \overline{X} is the mean of variable X . If the degree of anisotropy of Y_{2D} is small, such as for stratocumulus and cumulus, we use $E_{2D}^*(k)$ and if not, such as for cirrus clouds, $E_{2D}^{**}(k)$. Nonetheless, the user can also choose one of these methods.

Finally, the new 2D *local* optical depth (or the 2D new ice water content Y_{2D}^{new}) at the given cloud layer is computed by keeping the real part of the inverse 2D Fast Fourier Transform of the new quantity:

$$\widehat{Y_{2D}^{new}}(k) = E_{2D}^*(k) \exp(i\phi_{2D}(k)) \text{ or } \widehat{Y_{2D}^{new}}(k) = E_{2D}^{**}(k) \exp(i\phi_{2D}(k)) \quad (23)$$

But as a result, the distribution of Y_{2D}^{new} is not the same Y_{2D} at the given cloud layer, and the equality between the estimated spectral slope μ_{1D} of Y_{2D}^{new} and the required values β_{1D} is not always guaranteed. Therefore, we have to redo an "amplitude adaptation", as explained in Venema et al. (2006), and to iterate the process explained in this section by changing the value of β_{1D} in Eq. (21) or Eq. (22), until the estimated value μ_{1D} reaches the required value within a few percent.

15

2.2.3 Implementation

We describe here the part of the 3DCLOUD algorithm that establishes the cloud field mean optical depth $\overline{\tau}$ (IWC), the inhomogeneity parameter ρ_τ (or ρ_{IWC}) and the spectral exponent β_{1D} .

For stratocumulus and cumulus clouds, the algorithm is the following:

1) Transformation of $LWC(x, y, z)$ to $\tau'_{3D}(x, y, z)$ with Eq. (10). Effective radius can be set to 10 μm for example.

2) Application of the algorithm explained in Sect. 2.2.2 in order to constrain β_{1D} of each cloudy layer of $\tau'_{3D}(x, y, z)$. We obtain $\tau''_{3D}(x, y, z)$.

- 1 3) Computation of optical depth $\tau'(x, y)$ from $\tau''_{3D}(x, y, z)$ (Eq. (11)).
- 2 4) Transformation of $\tau'(x, y)$ to $\tau''(x, y)$ with the help of the algorithm explained in Sect.
- 3 2.2.1 in order to constrain $\bar{\tau}$ and ρ_{τ} values.
- 4 5) Transformation of $\tau''(x, y)$ to $\tau'''(x, y)$ with the algorithm explained in Sect 2.2.2 in order
- 5 to control β_{1D} value.
- 6 6) Normalization of $\tau'''(x, y)$ to the required $\bar{\tau}$ value, in order to obtain $\tau_{3D}(x, y, z)$.
- 7 For cirrus clouds, the algorithm is as follows:
- 8 1) Transformation of $IWC(x, y, z)$ to $IWC'(x, y, z)$ with the algorithm explained in Sect.
- 9 2.2.1 in order to constrain \overline{IWC} and ρ_{IWC} values.
- 10 2) Application of the algorithm explained in Sect. 2.2.2 in order to constrain β_{1D} of each cloud
- 11 layer of $IWC'(x, y, z)$. We obtain $IWC''(x, y, z)$.
- 12 3) Transformation of $IWC'''(x, y, z)$ to $IWC_{3D}(x, y, z)$ with the algorithm explained in Sect.
- 13 2.2.1 in order to constrain \overline{IWC} and ρ_{IWC} values.

14

15 **2.3 Differences between 3DCLOUD, IAFFT method and Cloudgen models**

16 Both IAFFT (Venema et al., 2006) and Cloudgen (Hogan and Kew, 2005) models are purely
 17 stochastic Fourier based approaches that are able to generate synthetic or surrogate cloud. On
 18 the contrary, 3DCLOUD solves, in a first step, basic atmospheric equations, in order to
 19 generate an intermediate cloud field. In its second step, as for both IAFFT and Cloudgen
 20 models, it uses Fourier tools (manipulation of energy and phase in frequency space) and
 21 amplitude adaptation (manipulation of distributions) in order to generate the final cloud field.
 22 IAFFT and Cloudgen are designed to simulate stratocumulus/cumulus fields for the first and
 23 cirrus fields for the second, when 3DCLOUD is able to simulate stratocumulus, cumulus and
 24 cirrus field within the same framework.

1 More specifically, the IAFFT method is designed to generate surrogate clouds having both
2 the amplitude distribution and power of the original cloud (2D LWC from 1D LWP
3 measurement, 3D LWC from 2D LWC fields or 3D LWC from 3D fields generated by LES).
4 It needs LES inputs or measurements. As explained in Venema et al. (2006), stratocumulus
5 often display beautiful cell structures, similar to Bénard convection, and LES clouds show
6 such features. But their 3D IAFFT surrogates show these much less and do not show
7 fallstreak or a filamentous structure. Due to the specific manipulations of Fourier coefficients
8 presented in the paper, we show that 3DCLOUD is able to simulate the cell structure of
9 stratocumulus (see Fig. 7c and Fig. 8), the filamentous structure of cirrus (see Fig. 13) and the
10 cirrus fallstreaks (see Fig. 14 and Fig. 15) relatively well. Moreover, the objective of
11 3DCLOUD is not to provide many surrogate clouds with the same amplitude distribution and
12 power spectrum from an LES original cloud, but to provide 3D LWC (or optical depth) with
13 the required cloud coverage, the $-5/3$ spectral slope (often observed in real clouds), the mean
14 value of the gamma distribution of the optical depth and the inhomogeneity parameter, all
15 these parameters being very pertinent for radiative transfer.

16 Cloudgen is designed to simulate surrogate cirrus with the cirrus specific structural properties:
17 fallstreak geometry and shear-induced mixing. It first generates a 3D fractal field by
18 performing an inverse 3D Fourier transform on a matrix of simulated Fourier coefficients
19 with amplitude consistent with observed 1D spectra. Then random phases are generated for
20 the coefficient allowing multiple cloud realizations with the same statistical properties.
21 Horizontal slices from the domain are manipulated in turn to simulate horizontal displacement
22 and to change the spectra with height. The final field is scaled to produce the observed mean
23 and fractional standard deviation of ice water content. 3DCLOUD does not use a 3D fractal
24 field, but a 3D IWC field simulated by the simplified atmospheric equation set. Therefore,
25 cloud structures due to wind shear are physically obtained by taking into account the
26 advection (a nonlinear term in momentum equation) rather than by a linear horizontal
27 displacement of phase. Afterwards, in the current version of 3DCLOUD, for each level, 2D
28 horizontal slices of this 3D IWC are manipulated in 2D Fourier domain in such a way that the
29 Fourier coefficient amplitude is consistent with the 2D spectra of the simulated IWC, with the
30 constraint that the 1D spectral slope is equal to $-5/3$ (this value can be change easily in future
31 version of 3DCLOUD). At each level, the 2D phase for the coefficient is kept unchanged.
32 Finally, the mean value of the 3D IWC and the inhomogeneity parameter are adjusted. As
33 explained by Hogan and Kew (2005), it is difficult with Cloudgen to generated anisotropic

1 cirrus structure such as roll-like structure near cloud top. 3DCLOUD, using physically based
2 equations, allows simulating such kinds of anisotropy, as for example, 3DCLOUD Kelvin-
3 Helmholtz wave breaking (see Fig. 14).

4

5 **3 Comparison between 3DCLOUD and large-eddy simulation (LES) outputs**

6 The objective of this section is to check that the basic atmospheric equations used in
7 3DCLOUD (see Sect. 2.1.1) are solved correctly. We compare 3DCLOUD and LES outputs
8 found in the scientific literature for marine stratocumulus, cumulus and cirrus regimes. Note
9 that assimilation techniques of meteorological profiles and of cloud coverage (see Sect. 2.1.2)
10 are not used here, except in Sect 3.4.

11 The test cases come from the output LES numerical files provided by the Global Water and
12 Energy Experiment (GEWEX) Cloud System Studies (GCSS) Working Group 1 (WG1) and
13 Working Group 2 (WG2), easily downloadable from the web. They are often used as a
14 benchmark. We choose the DYCOMS2-RF01 case (the first Research Flight of the second
15 Dynamics and Chemistry of Marine Stratocumulus) for the marine stratocumulus regime
16 (Stevens et al., 2005), the BOMEX case (Barbados Oceanographic and Meteorological
17 Experiment) for the shallow cumulus regime (Siebesma et al., 2003), and the ICMCP case
18 (Idealized Cirrus Model Comparison Project) for cirrus regimes (Starr, 2000).

19

20 **3.1 DYCOMS2-RF01 (GCSS-WG1) case**

21 We remember briefly the conditions of simulations and configurations, explained in detail in
22 Stevens et al. (2005). A 4-h simulation on a horizontal grid of 96 by 96 points with 35-m
23 spacing between grid nodes was required. Vertical spacing was required to be 5 m or less. In
24 3DCLOUD, we thus set $N_x = N_y = 96$ and $N_z = 240$, $L_x = L_y = 3.5$ km and $L_z = 1200$ m, so
25 that $\Delta x = \Delta y \approx 36.5$ m and $\Delta z = 5$ m. Initial profiles of the liquid water potential temperature
26 θ_l and of the total water mixing ratio q_t are $\theta_l = 289.0$ K and $q_t = 9.0$ g/kg if $z \leq z_i$ and
27 $\theta_l = 297.5 + (z - z_i)^{1/3}$ K and $q_t = 1.5$ g/kg if $z > z_i$. Other required forcings include
28 geostrophic winds ($U_g = 7$ m/s and $V_g = -5.5$ m/s), divergence of the large-scale winds (
29 $D = 3.75 \times 10^{-6} \text{ s}^{-1}$), surface sensible heat flux (15 W/m^2) and surface latent heat flux (115

1 W/m^2). The momentum surface fluxes where the total momentum is specified by setting
2 $u^* = 0.25 \text{ m/s}$ and the radiation schemes is based on a simple model of the net longwave
3 radiative flux (see Eq. (3) and Eq. (4) in Stevens et al., 2005).

4 Figure 2 shows the evolution of the mean cloud top height, the mean cloud base height, the
5 cloud coverage and the liquid water path from the master ensemble and for 3DCLOUD during
6 the 4-h simulations. Even though we can notice slight discrepancies between 3DCLOUD and
7 master ensemble results in the first 2 hours ("spinup" period), 3DCLOUD results are quite
8 consistent with master ensemble results, especially at the end of the simulation. Nevertheless,
9 3DCLOUD tends to generate a lower cloud height than the mean results with a higher liquid
10 water path.

11 Figure 3 shows the mean profiles averaged over the fourth hour of the longwave net flux, the
12 liquid water potential temperature, the total water mixing ratio, the liquid water mixing ratio,
13 the horizontal velocity components, and the air density. Even though the 3DCLOUD
14 longwave net flux is smaller compared to master ensemble, again 3DCLOUD results are quite
15 consistent with other results for all the variables.

16

17 **3.2 BOMEX (GCSS-WG1) case**

18 For the BOMEX case (Siebesma et al., 2003), a 6-h simulation on a horizontal grid of 64 by
19 64 points with 100-m spacing between grid node was required. Vertical spacing was required
20 to be 40 m. In 3DCLOUD, we set thus $N_x = N_y = 64$ and $N_z = 76$ with $L_x = L_y = 6.4 \text{ km}$ and
21 $L_z = 2980 \text{ m}$, so $\Delta x = \Delta y = 100 \text{ m}$ and $\Delta z \approx 39.2 \text{ m}$. Initial profiles of the liquid water potential
22 temperature θ_l and the total water mixing ratio q_t and the other requirement including
23 geostrophic winds, divergence due to the subsidence, surface sensible heat flux, surface latent
24 heat flux, momentum surface fluxes, moisture large scale horizontal advection term and
25 longwave radiative cooling (radiative effects due to the presence of clouds are neglected) are
26 presented in appendix B in Siebesma et al., 2003).

27 Figure 4 shows the evolution of the cloud coverage and the liquid water path from the master
28 ensemble and for 3DCLOUD during the 6-h simulation. We can notice the small value of the
29 cloud coverage (less than 10%). 3DCLOUD results are quite consistent with the master

1 ensemble results, even if the simulated 3DCLOUD liquid water path (LWP) may be too low
2 at the end of the simulation.

3 Figure 5 shows mean profiles, averaged over the fifth hour of the cloud coverage, potential
4 temperature, water vapour mixing ratio, liquid water mixing ratio, horizontal velocity
5 components, and air density. The 3DCLOUD results are again quite consistent with the
6 master ensemble results. We note, however, that the 3DCLOUD cloud coverage and liquid
7 water mixing ratio are smaller at all heights. We also see small differences (less than 1 m/s)
8 for the wind velocity below 500 m, and for the potential temperature (less than 1K) and water
9 vapour mixing ratio (less than 1g/kg) for altitudes 1,800 m.

10

11 **3.3 ICMCP (GCSS-WG2) case**

12 For the cirrus case detailed in Starr et al. (2000), the baseline simulations include night-time
13 "warm" cirrus and "cold" cirrus cases where cloud top initially occurs at -47°C and -66°C ,
14 respectively. The cloud is generated in an ice super-saturated layer with a geometric thickness
15 around 1 km (120% in 0.5 km layer) and with a neutral ice pseudo-adiabatic thermal
16 stratification. Cloud formation is forced via an imposed diabatic cooling over a 4-h time span
17 followed by a 2-h dissipation stage without cooling. All models simulate radiative transfer,
18 contrary to 3DCLOUD. In 3DCLOUD, we set $N_x = N_y = 60$ and $N_z = 140$ with
19 $L_x = L_y = 6.3$ km and $L_z = 14$ km, so that $\Delta x = \Delta y = 105$ m and $\Delta z \approx 100$ m.

20 Figure 6 shows the evolution of the ice water path (IWP) from the master ensemble and for
21 3DCLOUD during the 6-h simulation. In a general way, most of the tested models and
22 3DCLOUD have similar behaviour: indeed, the IWP increases during the first 4-h simulation
23 (cirrus formation due to imposed cooling) and decreases after (cirrus dissipation due to non-
24 imposed cooling). The IWP range of the tested models is very large (factor of 10), but we can
25 notice that 3DCLOUD behaviour is closer to bulk microphysics models behaviours,
26 especially for "warm cirrus".

27 For "cold" cirrus, the 3DCLOUD IWP is smaller than most participating models during all the
28 simulation duration. It is probably because 3DCLOUD does not account for the radiative
29 transfer, as opposed to the participating models. Indeed, neglecting cirrus top cooling due to

1 radiative processes restricts the formation of thin "cold" cirrus. This radiative diabatic effect is
2 probably less important for the "warm" cirrus because the latent heat diabatic effect is larger.

3

4 **3.4 Comparison between 3DCLOUD and BRAMS for the DYCOM2-RF01 case**

5 In order to underscore differences between 3DCLOUD and LES for comparable scenes, we
6 choose again the well documented DYCOMS2-RF01 case. Snapshots can be found, for
7 example, in Stevens et al. (2005) and in Yamaguchi and Feingold (2012). We performed the
8 4h simulations of the DYCOMS2-RF01 case with 3DCLOUD and with the Brazilian
9 Regional Atmospheric Modelling System (BRAMS v4) model (Pielke et al., 1992 ; Cotton et
10 al., 2003). BRAMS simulations were provided by G. Penide (Penide et al., 2010). The
11 BRAMS model is constructed around the full set of nonhydrostatic, compressible equations.
12 The cloud microphysics parameterization is based on a two-moment scheme (Meyers et al.,
13 1997). Subgrid scale fluxes are modeled following Deardroff (1980). The base calculations
14 are performed on a $100 \times 100 \times 100$ point mesh with a step time of 0.3 s.

15 Figure 7 shows the instantaneous cloud-field snapshots of the pseudo albedo (see definition in
16 Sect. 4) at four hours simulated by (a) the UCLA-0 model (picture taken from Stevens et al.,
17 2005), (b) the BRAMS model, both configured following the DYCOMS2-RF01 case (Stevens
18 et al., 2005) and (c) from 3DCLOUD with assimilation of meteorological profiles based on
19 the DYCOMS-RF01 case. Both BRAMS and 3DCLOUD cases are drawn from simulations
20 where $\Delta_x = \Delta_y = 40$ m and $\Delta_z = 12$ m. These three snapshots of cloud fields are characterized
21 by closed cellular convection with large cloud cover, as argued in Yamaguchi and Feingold
22 (2012), who did simulation of DYCOMS-RF01 case with the LES mode of the Advanced
23 Research WRF model. Figure 7 also shows the power spectra computed following the x and y
24 directions and then averaged, for BRAMS and 3DCLOUD optical depth fields. The
25 3DCLOUD optical depth spectral slope is close to $-5/3$ in the $[L_{out}; 1/(2\Delta x)]$ m^{-1}
26 wavenumber range, as expected, because of the statistical adjustment performed in the second
27 step of the 3DCLOUD algorithm. By contrast, the BRAMS optical depth spectral slope is
28 close to $-5/3$ only in the $[2 \times 10^{-3}; 5 \times 10^{-3} \approx 1/(5\Delta x)]$ m^{-1} wavenumber range. Depending
29 on their degree of sophistication, LES do not always guarantee cloud invariant scale
30 properties at the larger wavenumbers. Indeed, Bryan et al. (2003) have shown, that for the
31 finite-difference model, the vertical wind velocity spectral slope is steeper than $-5/3$ for scales

1 shorter than $6\Delta x$. Table 1 shows the computation performance of 3DCLOUD and BRAMS.
2 For this specific case, 3DCLOUD simulation is thirty times faster than BRAMS simulation.

3 **4 Examples of 3DCLOUD possibilities**

4

5 In this section, we present cloud fields generated by 3DCLOUD with the assimilation of
6 idealized meteorological profiles and fractional cloud coverage defined by the user. We also
7 show the effect of the outer scale L_{out} and the inhomogeneity parameter of optical depth ρ_τ
8 on the generated optical depth field. We also give an example of cirrus clouds with
9 fallstreaks. In order to have a spatial representation of the clouds as seen from above, we
10 choose to show the so-called pseudo-albedo α defined as:

$$11 \quad \alpha = \frac{(1-g)\tau}{2+(1-g)\tau} \quad (23)$$

12 where the asymmetry parameter g is set to 0.86 and τ is the optical depth.

13 **4.1 Stratocumulus and cumulus fields with assimilation of meteorological** 14 **profiles based on DYCOMS2-RF01 and BOMEX cases.**

15 We choose to simulate stratocumulus and cumulus LWC in the context of DYCOMS2-RF01
16 and BOMEX cases. With this aim, we assimilate temperature and humidity initial profiles for
17 stratocumulus and cumulus given by Stevens et al. (2005) and Siebesma et al. (2003),
18 respectively. However, in order to mimic the sensible and latent heat, these profiles have to be
19 slightly modified. At sea surface ($z=0$), for stratocumulus (DYCOMS2-RF01 case), the
20 liquid potential temperature and total mixing ratio are set to 290 K and 10 g/kg, respectively
21 (instead of 289 K and 9 g/kg, respectively). For cumulus (BOMEX case), the liquid potential
22 temperature is set to 299.7 K instead of 298.7 K. In addition, wind profiles assimilated by
23 3DCLOUD are those computed by the master ensemble at the end of simulation.

24 **4.1.1 Effects of numerical spatial resolution**

25 The effects of the numerical spatial resolution on 3DCLOUD simulations are presented
26 herein. Figure 8 shows pseudo-albedo and cross sections of the vertical velocity and cloud
27 water at the end of the simulation for the stratocumulus case based on the DYCOMS2-RF01
28 experiment. It also shows the mean profiles of potential temperature, liquid water mixing

1 ratio, horizontal velocity components, and vapour water mixing ratio for different numerical
2 spatial resolutions $\Delta x = \Delta y = 200$ m, 100 m, 50 m and 25 m. Horizontal extensions $L_x = L_y$ are
3 set to 10 km and vertical resolution Δz to 24 m for all simulations. Figure 9 is the same as
4 Fig. 8, but for the cumulus case with assimilation of meteorological profiles based on the
5 BOMEX case. The vertical resolution Δz is set to 38.5 m in this last case.

6 It is obvious that change in the horizontal mesh leads to a more pleasant and detailed flow
7 visualization but there is no significant impact on the mean statistics of the simulated
8 temperature vertical profile, water vapour mixing ratio and wind velocity. The water mixing
9 ratio simulated by 3DCLOUD for the DYCOMS2-RF01 case is very close to the mean profile
10 averaged over the fourth hour and provided by the master ensemble, even if the vertical
11 resolution used in this section is only $\Delta z = 38.5$ m compared to $\Delta z = 5$ m in Sect. 3.1. For the
12 BOMEX case, the water mixing ratio simulated by 3DCLOUD changes as a function of the
13 numerical spatial resolution. This behaviour is quite understandable as results drawn on Fig. 8
14 and Fig. 9 are snapshots at the end of the 3DCLOUD simulation and not average results over
15 1 hour as done on Fig. 3 and Fig. 5. Moreover, BOMEX meteorological conditions cause time
16 dependent cumulus fields, contrary to DYCOMS2 meteorological conditions that cause more
17 stationary stratocumulus fields.

18 In addition, it is expected for the BOMEX case, that cloud spacing converges at high spatial
19 resolution. In order to investigate it, we defined an estimator of the cloud spacing called the
20 mean distance D_{mean} . To compute D_{mean} , the 3D LWC is vertically projected on the 2D x-
21 y plan in order to obtain the 2D binary image of the cloud coverage with free cloud areas set
22 to 0 and cloudy areas set to 1. Then we compute the mean distance between the cloud cell for
23 the x and y directions to obtain D_{mean} . Figure 10 shows time series of D_{mean} for different
24 horizontal spatial resolution ($\Delta x = \Delta y = 192, 100, 50, 25, 12.5$ and 8.3 m) with a constant
25 vertical resolution ($\Delta z = 38.5$ m), for cumulus cloud fields simulated by 3DCLOUD after
26 assimilation of the BOMEX case meteorological profiles. The main difference between these
27 simulations and the BOMEX case simulation is the smaller horizontal extension $L_x = L_y = 5$
28 km instead of 10 km in order to access high numerical spatial resolution $\Delta x = 8.3$ m ($N_x =$
29 $N_y = 600, N_z = 70$). Cumulus clouds appear 10 to 20 min after the beginning of the
30 simulation. After 1 h of simulation, D_{mean} is relatively constant with time, meaning that
31 3DCLOUD has converged. The mean distance averaged over the last half-hour of the 2h
32 simulation $\overline{D_{mean}}$, is also presented in Fig. 10 as a function of the numerical spatial

1 resolution Δx . $\overline{D_{mean}}$ is relatively constant for a spatial resolution Δx smaller than 20 m,
2 showing that BOMEX cloud spacing converges for spatial resolution close to $\Delta x = 10$ m, a
3 value smaller than $\Delta x = 25$ m used in Fig. 9d.

4 Table 1 shows the time step, process time for one time step and process time for 2h-
5 simulation with 3DCLOUD model, as a function of the numerical resolution. DYCOMS2-
6 RF01 and BOMEX cases are presented. The process time for 2h-simulation is indicated
7 because 3DCLOUD algorithm convergence is achieved after 2 h (or less) of simulation for
8 stratocumulus, cumulus and cirrus regimes (see Fig. 10 for cumulus case). For both cases, the
9 smaller the spatial resolution, the smaller the step time and the larger the process time. A
10 comparison between 3DCLOUD and BRAMS LES computation time for a specific
11 DYCOMS2-RF01 case is added (see Sect. 3.4). For this specific case, 3DCLOUD simulation
12 is thirty times faster than BRAMS simulation. Note that 3DCLOUD (Matlab code) runs on a
13 personal computer with Intel Xeon E5520 (2.26 GHz) and BRAMS (Fortran code) runs on a
14 PowerEdge R720 with Intel Xeon E5-2670 (2.60 GHz), both of them having a single-
15 processor configuration.

16

17 **4.1.2 Assimilation of the fractional cloud coverage C**

18 Results shown in Fig. 11 are the same as Fig. 8 but with the addition of the cloud coverage
19 assimilation $C = 99\%$, $C = 80\%$, $C = 50\%$ and $C = 20\%$. Horizontal extensions L_x and L_y
20 are set to 10 km and vertical resolution Δz is set to 24 m.

21 They show that 3DCLOUD is able to assimilate correctly fractional cloud coverage of
22 stratocumulus for very different values of C , even though the extreme example with
23 $C = 20\%$ is a fair weather cumulus field rather than a stratocumulus. For each value of C
24 assimilated, it is interesting to note that cloud base and cloud top heights are still localised
25 around 600 m and 800 m, respectively. Temperature vertical profiles are almost unchanged.
26 The water mixing ratio vertical profiles decrease with the assimilated C value.

27 **4.1.3 Effect of the outer scale L_{out} and inhomogeneity parameter ρ_τ on the** 28 **optical depth field**

29 We saw that 3DCLOUD can, at the end of step 1, simulate stratocumulus and cumulus fields
30 with enough coherent statistics profiles. However, optical depth (for stratocumulus and

1 cumulus) or IWC (for cirrus) generated during step 1 of 3DCLOUD does not show scale
 2 invariant properties observed in real cloud and often characterised by the spectral exponent
 3 β_{ID} close to $-5/3$. As described in Sect. 2.2, it is the main task of the step 2 of 3DCLOUD, in
 4 addition to the adjustment of the mean and standard deviation of optical thickness or IWC.
 5 We focus on the DYCOMS2-RF01 case at the spatial resolution $\Delta x = 50\text{m}$ (Fig. 8c). The
 6 effective radius R_{eff} is set to $10\mu\text{m}$ to compute optical depth from liquid water content. The
 7 mean optical depth of this initial field is set to 10 and we change the inhomogeneity parameter
 8 ρ_τ and the outer scale L_{out} to 0.2 and 1 km, respectively, for case 1 to 0.7 and 1 km for case 2
 9 and to 0.7 and 10 km for case 3. Figure 12 shows pseudo-albedo, mean power spectra,
 10 probability density function of optical depth fields, mean vertical profiles of the horizontally
 11 averaged optical depth for the three cases and a volume rendering of optical depth.

12 First, we notice that the pseudo-albedo of the initial optical depth field (see Fig. 12a) is
 13 smoother than the pseudo-albedo of case 1, 2, and 3. Between cases 1 and 2, we clearly see an
 14 increase in heterogeneity as case 1 is a quasi-homogenous stratocumulus with a small value of
 15 $\rho_\tau = 0.2$ and case 2 is more inhomogeneous with a larger value of $\rho_\tau = 0.7$. Between cases 2
 16 and 3, we can see the effect of the outer scale. In accordance with smooth variations, the
 17 spectral slope of the initial optical depth is close to -3 for the $[10^{-3} : 10^{-2}] \text{ m}^{-1}$ wavenumber
 18 range (Fig. 12e). Cases 1, 2 and 3 present the proper spectral slope value of $-5/3$. For cases 1
 19 and 2, this slope is obtained for the $[10^{-3} : 10^{-2}] \text{ m}^{-1}$ wavenumber range, which is coherent
 20 with the imposed value of outer scale $L_{out} = 1 \text{ km}$. For case 3, $L_{out} = 10 \text{ km}$, so the spectral
 21 slope should be $-5/3$ on the $[10^{-4} : 10^{-2}] \text{ m}^{-1}$ wavenumber range. However, we note that this
 22 spectral slope value is achieved only for the $[5 \times 10^{-3} : 10^{-2}] \text{ m}^{-1}$ wavenumber range, because
 23 we keep the phase angles unchanged in the 3DCLOUD algorithm.

24 In Fig. 12f, we represent the optical depth distributions. The initial optical depth distribution
 25 does not follow a common distribution, whereas the optical depth distribution for cases 1 and
 26 2 are log-normal. Indeed, in the 3DCLOUD algorithm, a gamma distribution for the optical
 27 depth is imposed. For case 2 and 3, optical depth distributions are very close, even if the outer
 28 scales are different. Thus, changing the L_{out} value does not affect significantly the shape of

1 optical depth distribution. In Fig. 12g, we can see that the horizontal mean optical depth
2 profiles are quasi identical for all cases.

3 These results show undeniably the flexibility of the 3DCLOUD algorithm. Indeed, in step 2,
4 3DCLOUD is able, by mapping a theoretical gamma-distributed optical depth onto the optical
5 depth field simulated at step1, to adjust, quasi-independently, the optical depth mean value,
6 the inhomogeneity parameter value of optical depth and the spectral slope value of optical
7 depth for $[1/L_{out} : 1/2\Delta x]$ m^{-1} wavenumber range.

8

9 **4.2 Cirrus fields examples**

10 **4.2.1 Cirrus fields with assimilation of idealized meteorological profiles**

11 Including some modifications presented in Sect. 2.1.1, 3DCLOUD is also able to generate
12 cirrus cloud. We briefly present in this section an example of ice water content (IWC) of
13 cirrus with fallstreaks. For cirrus, we chose to generate IWC field instead of optical depth
14 field as for stratocumulus or cumulus.

15 Figure 13 shows idealized vertical profiles of potential temperature, relative humidity, and
16 horizontal velocity components assimilated by 3DCLOUD as well as the ice water path (IWP)
17 simulated at step 1 by 3DCLOUD. It also shows the IWP simulated by 3DCLOUD during
18 step 2, the initial and corrected mean power spectra, the initial and corrected probability
19 density functions and the IWC volume rendering. Horizontal extensions $L_x = L_y$ and vertical
20 extension L_z are set to 10 km and 12.5 km, respectively. Horizontal resolutions $\Delta x = \Delta y$ and
21 vertical resolution Δz are set to 24 m and 83.3 m, respectively. \overline{IWC} is set to the value
22 obtained at the end of step 1 (0.54 mg/m^3). The inhomogeneity parameter ρ_{IWC} is set to 1.0
23 and the outer scale L_{out} to 1 km.

24 Initial meteorological profiles assimilated by 3DCLOUD have been constructed in such a way
25 that thin cirrus is generated between 9.5 km and 10.5 km with fallstreaks. Vertical profiles of
26 potential temperature, and especially their vertical gradients under and above the cirrus are
27 based on those proposed by Liu et al. (2003). In order to generate instabilities due to radiative
28 cooling (not simulated by 3DCLOUD), we imposed a null vertical gradient of the potential
29 temperature near the cirrus top height. We imposed a mean relative humidity with respect to

1 ice (RHI) of 104 % between 9.5 km and 10.5 km. Just above the cloud, RHI is set to 50%
2 then 20% near 12 km in altitude. Under the cirrus, RHI decreases with height to 85% near 8
3 km. To generate fallstreaks, we imposed larger wind shear inside the cirrus than under the
4 cirrus.

5 In Fig. 13, we note that IWP obtained after step 1 is smoother than IWP obtained after step 2,
6 and that the initial IWC spectral slope value after step 1 is much smaller (around -5.5) than
7 the corrected IWC spectral slope after step 2 (around -1.6) in the $[10^{-3}:2\times 10^{-2}]$ m^{-1}
8 wavenumber range. For wavenumber smaller than $1/L_{out} = 10^{-3} \text{ m}^{-1}$, the power spectra are
9 constant. The corrected IWC probability distribution is exponential-like distribution after step
10 2. This is due to the larger value of $\rho_{IWC} = 1.0$ used in this example, compared to $\rho_{\tau} = 0.7$
11 used for stratocumulus in Sect 4.1.3.

12

13 **4.2.2 Cirrus field and wind shear**

14 We investigate briefly the aspect of cloud organization due to wind shear with 3DCLOUD
15 model and with other stochastic models. We focus on the work of Marsham and Dobbie
16 (2005) and of Hogan and Kew (2005). These two studies are very pertinent together. Indeed,
17 based on RADAR retrievals of IWC from the Chilbolton 94 GHz RADAR on 27 December
18 1999, which shows a strongly sheared ice cloud (named hereafter RC99 case), Marsham and
19 Dobbie (2005) investigated shear effects by simulating the RC99 case with the UK Met office
20 LES. In contrast, Hogan and Kew (2005) used their Cloudgen model, a 3D stochastic cloud
21 model being able to simulate the structural properties of ice clouds. To configure 3DCLOUD
22 in order to simulate the RC99 case, we assimilate meteorological profiles (potential
23 temperature, horizontal wind velocity) based on those drawn in Fig 2 in Marsham and Dobbie
24 (2005). We run also the RC99a case with no wind (and therefore no wind shear), and the
25 RC99b case where the potential temperature profile (drawn in Fig 15 in Marsham and
26 Dobbie, 2005) reduces atmospheric stability in order to give more extensive Kelvin-
27 Helmholtz wave braking. All our simulations are done with $N_x = N_y = 200$ and $N_z = 66$
28 and $\Delta_x = \Delta_y = 250$ m and $\Delta_z = 120$ m. Horizontal extensions are $L_x = L_y = 50$ km and
29 vertical extension is $L_z = 8$ km between 4 km and 12 km. Note that 3DCLOUD, Marsham
30 and Dobbie (2005) and Hogan and Kew (2005) numerical resolution are $\Delta_x = \Delta_y = 250$ m,

1 $\Delta_x = 100\text{m}$ and $\Delta_x \approx 780\text{ m}$, respectively. Note also that 3DCLOUD, Marsham and Dobbie
2 (2005) and Hogan and Kew (2005) horizontal extensions are $L_x = L_y = 50\text{ km}$, $L_x = 50\text{ km}$
3 and $L_x = L_y = 200\text{ km}$.

4 Figure 14 shows a 2D vertical slice of 3DCLOUD IWC at an angle parallel to the wind of the
5 RC99a case, the RC99 case and the RC99b case. Note that the 3DCLOUD fields are smooth
6 because they are obtained at the first step of the algorithm. These three snapshots are very
7 similar to those presented in Marsham and Dobbie (2005), allowing us to confirm that our
8 basic atmospheric equations are correctly solved. In Fig. 14a, we can see small structures (few
9 km) at above 7 km, due to radiative cooling at the cloud top and latent heat release in the
10 updraughts. Below, we can observe fallstreaks advected (or not if there is no wind) relative to
11 their source in the convective layer by the shear. The shear homogenizes the fallstreaks.
12 Figure 14b clearly shows that 3DCLOUD simulations at the first step of the algorithm
13 homogenize the fallstreaks a lot, certainly too much compared to the RADAR retrievals of
14 IWC from the Chilbolton 94 GHz RADAR on 27 December 1999 (see Fig. 1 in Hogan and
15 Kew, 2005). Figure 14c shows the RC99b case where 3DCLOUD model is able to simulate
16 Kelvin-Helmholtz wave breaking, a dynamic aspect difficult to simulate with purely
17 stochastic models.

18 Figures 15a and 15b are the same as Fig. 14b but 3DCLOUD fields are obtained at the second
19 step of the algorithm, with 1D spectral slope close to $-5/3$ from the outer scale $L_{out} = 15\text{ km}$
20 to the numerical scale $\Delta x = 250\text{ m}$. In Fig. 15a, the mean value of 3D IWC $\overline{IWC} = 0.07\text{ gm}^{-3}$
21 and inhomogeneity parameter $\rho_{IWC} = 0.4$ for cloudy voxels are those computed from the 3D
22 IWC field obtained at step one of the 3DCLOUD algorithm. In Fig. 15b, inhomogeneity
23 parameter ρ_{IWC} is a function of height. Its values are roughly estimated from the Fig. 2c in
24 Hogan and Kew (2005). Compared to Hogan and Kew (2005) simulations, 3DCLOUD
25 snapshots show more details in the convective layer above 7 km as it simulates relatively well
26 the convective cloud structures thanks to imposed numerical spatial resolution. By contrast to
27 Fig. 15a, Hogan and Kew (2005) simulations show more details in the layer under 7 km,
28 where the shear-induced mixing is important. In order to obtain such details in the layer under
29 7 km with 3DCLOUD, we have to constrain it with ancillary data: those provided by the
30 RADAR retrievals of IWC and shown on Fig. 2c in Hogan and Kew (2005). Indeed, if we
31 force, in the second step of 3DCLOUD algorithm, the vertical inhomogeneity parameter to
32 match the one estimated crudely from the RADAR retrievals, we obtain Fig. 15b. Details in

1 the layer under 7 km of this snapshot are quite similar to those obtained by Hogan and Kew
2 (2005).

3 Finally, Fig. 16, which is similar to Fig. 2 in Hogan and Kew (2005), shows vertical profiles
4 of the cloud fraction, the mean of logarithm of IWC for the cloudy voxels and the standard
5 deviation of logarithm of IWC for cloudy voxels computed from two 3DCLOUD fields
6 obtained at the second step of the algorithm for RC99 case. As for Fig. 15, inhomogeneity
7 parameter is $\rho_{IWC} = 0.4$ for the first cloud field and depends on height and it is derived from
8 RADAR retrievals for the second case. For both cloud fields, the cloud coverage is equal to 1
9 between 5 km and 10 km. RADAR retrievals of IWC shows that the cloud coverage is equal
10 to 1 only between 5.5 km and 7 km, and decreases to 0 at 10 km. However, as discussed in
11 Sect. 2.1.2, the current version of 3DCLOUD is not able to readily simulate fractional cloud
12 coverage in the cirrus regime. For both cloud fields, vertical profiles of the mean IWC are
13 quite similar and consistent with those retrieved from RADAR. The inhomogeneity parameter
14 vertical profile simulated by the current version of 3DCLOUD is too small, leading to a
15 smoothing of the layer under 7 km that can be improved if the vertical profile of the
16 inhomogeneity parameter is known.

17

18 **5 Conclusion**

19

20 3DCLOUD is a flexible three-dimensional cloud generator developed to simulate with a
21 personal computer and under Matlab environment, synthetic but realistic stratocumulus,
22 cumulus and cirrus cloud fields. Simplified dynamic and thermodynamic laws allow the
23 generation of realistic liquid or ice water content from meteorological profiles. The stochastic
24 process with the Fourier framework allow us to provide ice water content or optical depth
25 sharing similar statistical properties to those observed in real clouds such as the
26 inhomogeneity parameter (set by the user) and the invariant scale properties characterised by
27 a spectral slope close to $-5/3$ from the smaller scale (set by spatial resolution of grid
28 computation) to the outer scale (set by the user). In order to simulate cloud structures,
29 3DCLOUD solves simplified basic atmospheric equations and assimilates the cloud coverage
30 set by the user (only for the stratocumulus and cumulus regimes) and meteorological profiles
31 (pressure, humidity, wind velocity) defined by the user.

1 The 3DCLOUD outputs were compared to LES ones for three classical test cases. We chose
2 the case of DYCOMS2-RF01, the case of BOMEX , and the case of ICMCP. For these cases,
3 results show that 3DCLOUD outputs are relatively consistent with LES outputs, and confirm
4 that the chosen basic atmospheric equations of 3DCLOUD are solved correctly. We also show
5 that, under the condition that the user provides coherent meteorological profiles, 3DCLOUD
6 algorithm is able to assimilate them and generate realistic cloud structures.

7 3DCLOUD is a very interesting research tool to better understand 3D interactions between
8 cloudy atmosphere and atmospheric radiation, which is of primary importance in order to
9 make progress in the direct radiative problem (GCM context) and in the inverse radiative
10 problem (remote sensing context, development of the next generation of atmospheric
11 sensors). For example, 3DCLOUD was used to quantify the impact of stratocumulus
12 heterogeneities on polarized radiation measurements performed by POLDER/PARASOL
13 (Cornet et al., 2013) as well as the influence of cirrus heterogeneities on brightness
14 temperature measured by IIR/CALIPSO (Fauchez et al., 2013, 2014).

15 We still have to develop a stochastic process to generate 3D field of cloud effective radius. In
16 a longer term, investigations will focus on the generation of 3D mixed phase cloud and
17 eventually on the simulation of 3D rain rate. Another task will be to provide a FORTRAN
18 code of 3DCLOUD, assumed to be faster than the current Matlab code.

19

20

21

22

23

24

25

26

27

28

29

1 **Code availability**

2

3 The source code of the 3DCLOUD algorithm is available online at <http://wwwobs.univ->
4 [bpclermont.fr/atmos/fr/restricted](http://wwwobs.univ-bpclermont.fr/atmos/fr/restricted)

5 Please contact the authors for the password.

6

7

8

9

10

11

12

13

14

15

16

17

18

19

20

21

22

23

24

25

26

1 **Acknowledgements**

2 This work has been supported by the Programme National de Télédétection Spatiale (PNTS,
3 [http://www.insu.cnrs.fr/actions-sur-projets/pnts-programme-national-de-teledetection-
5 spatiale](http://www.insu.cnrs.fr/actions-sur-projets/pnts-programme-national-de-teledetection-
4 spatiale)), grant n° PNTS-2012-08 and by the Office National d'Etudes et de Recherches
6 Aérospatiales (the French aerospace laboratory, ONERA). The authors thank Pr. Wolfram
7 Wobrock and Pr. Valery Shcherbakov for the numerous fruitful discussions on physics and
8 atmospheric dynamics. We also thank the two reviewers whose remarks largely improved the
9 quality of this article.

1 **References**

- 2 Alexandrov, M. D., Marshak, A., and Ackerman, A. S.: Cellular statistical models of broken
3 cloud fields. Part I: Theory, *J. Atmos. Sci.*, 67, 2125-2151, doi:10.1175/2010JAS3364.1,
4 2010.
- 5 Asai, T.: A numerical study of the air-mass transformation over the Japan Sea in winter, *J.*
6 *Met. Soc. Japan*, 43, 1-15, 1965.
- 7 Barker, H. W. and Liu, D. M.: Inferring optical depth of broken clouds from Landsat data, *J.*
8 *Climate*, 8, 2620-2630, 1995.
- 9 Barker, H. W., Wiellicki B. A., and Parker, L.: A parameterization for computing grid-
10 averaged solar fluxes for inhomogeneous marine boundary layer clouds. Part II: validation
11 using satellite data, *J. Atmos. Sci.*, 53, 2304–2316, 1996.
- 12 Battaglia, A. and Mantovani, S.: Forward Monte Carlo computations of fully polarized
13 microwave radiation in non isotropic media, *J. Quant. Spectrosc. Rad. Transf.*, 95, 285-308,
14 2005.
- 15 Battaglia, A. and Tanelli, S.: DOMUS: DOppler MUltiple-Scattering Simulator, *IEEE Trans.*
16 *Geosci Rem. Sens.*, 49, 442-450, 2011.
- 17 Benassi, A., Szczap F., Davis, A. B., Masbou, M., Cornet, C., and Bleuyard, P.: Thermal
18 radiative fluxes through inhomogeneous cloud fields: A sensitivity study using a new
19 stochastic cloud generator, *Atmos. Res.*, 72, 291-315, 2004.
- 20 Bony, S. R., Colman, R., and Kattsov, V. M.: How well do we understand and evaluate
21 climate change feedback processes ?, *J. Climate*, 19, 3445-3482, 2006.
- 22 Bryan, G. H., Wyngaard, J. C., and Fritsch, J. M.: Resolution requirements for the simulation
23 of deep moist convection, *Mon. Wea. Rev.*, 131, 2394-2416, 2003
- 24 Cahalan, R. F.: Bounded cascade clouds albedo and effective thickness, *Nonlinear Proc.*
25 *Geophys.*, 1, 156-167, 1994.
- 26 Cahalan, R. F., Ridgway, W., Wiscombe, W. J., Bell, T. L., and Snider, J. B.: The albedo of
27 fractal stratocumulus clouds, *J. Atmos. Sci.*, 51, 2434–2455, 1994.
- 28 Carlin, B., Fu Q., Lohmann U., Mace G. G., Sassen K., and Comstock, J. M.: High cloud
29 horizontal inhomogeneity and solar albedo bias, *J. Climate*, 15, 2321-2339, 2002.

1 Chen, C. and Cotton, W. R.: A one-dimensional simulation of the stratocumulus-capped
2 mixed layer, *Bound-Layer Meteor.*, 25, 289–321, 1983.

3 Cheng, W. Y. Y., Wu, T., and Cotton, W. R.: Large-eddy simulations of the 26 November
4 1991 FIRE II cirrus case, *J. Atmos. Sci.*, 58, 1017-1034, 2001.

5 Clothiaux, E. E., Barker H. W., and Korolev, A. V.: Observing clouds and their optical
6 properties, in : *3D Radiative Transfer in Cloudy Atmospheres*, edited by Marshak A. and
7 Davis A. B., Springer, 93-152, 2004

8 Collins, W. D. and Satoh, M.: Simulating global clouds, past, present, and future, in: *Clouds*
9 *in the Perturbed Climate System*, edited by Heintzenberg, J. and Charlson R. J., MIT press,
10 469-486, 2009.

11 Cotton, W. R., Pielke, R. A., Walko, R. L., Liston, G. E., Tremback, C. J., Jiang, H.,
12 McAnelly, R. L., Harrington, J. Y., Nicholls, M. E., Carrio, G. G., and McFadden, J.P.:
13 RAMS 2001: Current status and future directions, *Meteorol. Atmos. Phys.*, 82, 5-29, 2001.

14 Cornet, C., Buriez, J.-C., Riedi, J., Isaka, H., and Guillemet, B.: Case study of inhomogeneous
15 cloud parameter retrieval from MODIS data, *Geophys. Res. Lett.*, 32, L13807,
16 doi:10.1029/2005GL022791, 2005

17 Cornet, C., Labonnote, L.-C., and Szczap, F.: Three-dimensional polarized Monte Carlo
18 atmospheric radiative transfer model (3DMCPOL): 3D effects on polarized visible
19 reflectances of a cirrus cloud, *J. Quant. Spectr. Radiative Transfer*, 111, 174-186,
20 doi:10.1016/j.jqsrt.2009.06.013, 2010.

21 Cornet, C., Szczap, F., Labonnote, L.-C., Fauchez, T., Parol, F., Thieuleux, F., Riedi, J.,
22 Dubuisson, P. and Ferlay, N.: Evaluation of cloud heterogeneity effects on total and polarized
23 visible radiances as measured by POLDER/PARASOL and consequences for retrieved cloud
24 properties , *AIP Conf. Proc.*, 1531, 99-102, doi: 10.1063/1.4804717 , 2013.

25 Davis, A. B., Marshak, A., Cahalan, R. F., and Wiscombe, W. J.: Multifractal
26 characterizations of non-stationarity and intermittency in geophysical fields, observed,
27 retrieved or simulated. *J. Geophys. Res.*, 54, 241–260, 1994.

28 Davis, A. B., Marshak, A., Wiscombe, W. J., and Cahalan, R. F.: Scale invariance of liquid
29 water distribution in marine stratocumulus: Part I. Spectral properties and stationarity issues.
30 *J. Atmos. Sci.* 53, 1538–1558, 1996.

- 1 Davis, A. B., Marshak, A., Cahalan, R. F., and Wiscombe, W. J.: The Landsat scale break in
2 Stratocumulus as a three-dimensional radiative transfer effect: implication for cloud remote
3 sensing. *J. Atmos. Sci.* 54, 241–259, 1997.
- 4 Davis, A. B., Marshak, A., Gerber, H., and Wiscombe, W. J.: Horizontal structure of marine
5 boundary layer clouds from centimeter to kilometer scales. *J. Geophys. Res.* 104, 6123–6144,
6 1999.
- 7 Deardorff, J. W.: Stratocumulus-capped mixed layers derived from a three-dimensional
8 model, *Bound.-Layer Meteor.*, 18, 495–527, 1980.
- 9 Di Giuseppe, F. and Tompkins, A. M.: Effect of spatial organisation on solar radiative
10 transfer in three dimensional idealised stratocumulus cloud fields, *J. Atmos. Sci.*, 60, 1774-
11 1794, 2003.
- 12 Emanuel K. A.: *Atmospheric Convection*, Oxford university press, 1994.
- 13 Evans, K. F. and Wiscombe, W. J.: An algorithm for generating stochastic cloud fields from
14 radar profile statistics, *Atmos. Res.*, 72, 263-289, 2004.
- 15 Fauchez, T., Cornet, C., Szczap F., and Dubuisson, P.: Assessment of cloud heterogeneities
16 effects on brightness temperatures simulated with a 3D Monte-Carlo code in the thermal
17 infrared, *AIP Conf. Proc.* Vol. 1531, 75-78, DOI: 10.1063/1.4804711, 2013
- 18 Fauchez, T., Cornet, C., Szczap, F., Dubuisson, P., and Rosambert, T.: Impacts of cirrus
19 clouds heterogeneities on TOA thermal infrared radiation, accepted to *Atmos. Chem. Phys.*,
20 2014.
- 21 Hill, P. G., Hogan R. J., Manners, J., and Petch, J. C.: Parametrising the horizontal
22 inhomogeneity of ice water content using CloudSat observations, *Q. J. R. Meteorol. Soc.*,
23 138, 1784-1793, 2012.
- 24 Hogan, R. J. and Kew, S. F.: A 3D stochastic cloud model for investigating the radiative
25 properties of inhomogeneous cirrus clouds, *Q. J. R. Meteorol. Soc.*, 131, 2585-2608, 2005.
- 26 Holton, J. R.: *An Introduction to Dynamic Meteorology*, Fourth edition, Elsevier academic
27 press, 2004.
- 28 Houze Jr., R. A.: *Cloud Dynamics*, Academic press, San Diego, 1993.

1 Illingworth, A. and Bony, S.R.: Observational strategies at meso- and large scales to reduce
2 critical uncertainties in future cloud changes, in : Clouds in the Perturbed Climate System,
3 edited by Heintzenberg, J. and Charlson R. J., MIT press, 511-530, 2009.

4 Kärcher, B. and Spichtinger, P.: Cloud-controlling factors of cirrus, in : Clouds in the
5 Perturbed Climate System, edited by Heintzenberg, J. and Charlson R. J., MIT press, 235-
6 268, 2009.

7 Kobayashi, T.: Effects due to cloud geometry on biases in the albedo derived from radiance
8 measurements, *J. Climate*, 6, 120-128, 1993.

9 Lafont, D. and Guillemet, B.: Subpixel fractional cloud cover and inhomogeneity effects on
10 microwave beam-filling error, *Atmos. Res.*, 72,149-168, doi: 10.1016/j.atmosres.2004.03.013,
11 2004.

12 Liou, K. N., *An introduction to atmospheric radiation*, Academic press, 2002.

13 Liu, H.-C., Wang, P. K., and Schlesinger, R. E.: A numerical study of cirrus clouds. Part II:
14 effects of ambient temperature, stability, radiation, ice microphysics, and microdynamics on
15 cirrus evolution, *J. Atmos. Sci.*, 60, 1097–1119, 2003.

16 Marshak, A., Davis, A., Wiscombe, W. J. , Ridgway, W., and Cahalan, R.: Biases in
17 shortwave column absorption in the presence of fractal clouds, *J. Climate*, 11, 431-446, 1998.

18 Mayer, B.: Radiative transfer in the cloudy atmosphere, *European Physical Journal*
19 *Conferences*, 1, 75-99, 2009.

20 Meyers, M. P., Walko, R. L., Harrington, J. Y., and Cotton, W. R.: New RAMS cloud
21 microphysics parameterization. Part II. The two-moment scheme, *J. Atmos. Res.*, 45, 3-39,
22 1997.

23 Moeng, C. H.: A large-eddy-simulation model for the study of planetary boundary-layer
24 turbulence, *J. Atmos. Sci.*, 41, 2052-2062, 1984.

25 Penide, G., Giraud, V., Bouniol, D., Dubuisson, P., Duroure, C., Protat, A., and Cautenet, S.:
26 Numerical simulation of the 7 to 9 September 2006 AMMA mesoscale convective system:
27 Evaluation of the dynamics and cloud microphysics using synthetic observations. AMMA
28 special issue, *Quart. J. Roy. Meteor. Soc.*, 136 (S1), 304-322, DOI 10.1002/qj.558, 2010.

1 Pincus, R. and Evans, K. F.: Computational cost and accuracy in calculating three-
2 dimensional radiative transfer: Results for new implementations of Monte Carlo and
3 SHDOM, *J. Atmos. Sci.*, 66, 3131-3146, 2009.

4 Pielke, R. A., Cotton, W. R., Walko, R. L., Tremback, C. J., Lyons, W.A., Grasso, L. D.,
5 Nieholls, M. E., Moran, M. D., Wesley, D. A., Lee, T. J., and Copeland, J. H.: A
6 comprehensive meteorological modelling system-RAMS, *Meteorol. Atmos. Phys.*, 49, 69-91,
7 1992.

8 Pielke, R. A.: *Mesoscale Meteorological Modeling*, Academic press, 2002.

9 Riddaway, R. W.: Numerical methods, available at : [www.ecmwf.int/newsevents/training/
10 rcourse_notes/NUMERICAL_METHODS/NUMERICAL_METHODS/Numerical_methods6
11 .html](http://www.ecmwf.int/newsevents/training/course_notes/NUMERICAL_METHODS/NUMERICAL_METHODS/Numerical_methods6.html) (last access: 10 January 2014), 2001.

12 Sassen, K., Wang L., Starr D. O. C, Comstock J. M., and Quante, M.: A midlatitude cirrus
13 cloud climatology from the facility for atmospheric remote sensing. Part V: Cloud structural
14 properties, *J. Atmos. Sci.*, 64, 2483-2501, 2007.

15 Siebesma, A. P., Bretherton, C. S., Brown, A., Chlond, A., Cuxart, J., Duynkerke, P. G.,
16 Jiang, H., Khairoutdinov, M., Lewellen, D., H-Moeng, C., Sanchez, E., Stevens, B., and
17 Stevens, D. E.: A Large-Eddy Simulation intercomparison study of shallow cumulus
18 convection , *J. Atmos. Sci.*, 60, 1201-1219, 2003.

19 Starr, D. O. C. and Cox, S. K.: Cirrus Clouds. Part I: A cirrus cloud model, *J. Atmos. Sci.*, 42,
20 2663–2681, 1985.

21 Starr, D. O. C., Benedetti, A., Boehm, M., Brown, P. R. A., Gierens, K. M., Girard, E.,
22 Giraud, V., Jakob, C., Jensen, E., Khvorostyanov, V. I., Koehler, M., Lare, A., Lin, R.-F.,
23 Maruyama, K., Montero, M., Tao, W.-K., Wang, Y., and Wilson, D.: Comparison of cirrus
24 cloud models: a project of the GEWEX Cloud System Study (GCSS) working group on cirrus
25 cloud system. Proceedings of the 13th International Conference on Cloud and Precipitation
26 (ICCP), Reno, NV, USA, 14–18 August 2000.

27 Stevens, B., H-Moeng, C., Ackerman A. S., Bretherton, C. S., Chlond, A., de Roode, S.,
28 Edwards, J., Golaz, J. C., Jiang, H., Khairoutdinov, M., Kirkpatrick, M. P., Lewellen, D. C.,
29 Lock, A. L., Müller, F., Stevens, D. E., Whelan, E., and Zhu, P.: Evaluation of large-eddy
30 simulations via observations of nocturnal marine stratocumulus, *Mon. Wea. Rev.*, 133, 1443–
31 1462, 2005.

1 Szczap, F., Isaka, H., Saute, M., Guillemet, B., and Ioltukhovski, A.: Effective radiative
2 properties of bounded cascade nonabsorbing clouds: Definition of the equivalent
3 homogeneous cloud approximation, *J. Geophys. Res.*, 105, D16, 20,617-20,634,
4 doi:10.1029/2000JD900146, 2000.

5 Szczap, F., Cornet, C., Alqassem, A., Gour, Y., Labonnote, C.-L., and Jourdan, O.:
6 A 3D polarized Monte Carlo LIDAR system simulator for studying effects of cirrus
7 inhomogeneities on CALIOP/CALIPSO measurements, *AIP Conf. Proc.*, 1531, 139-142, doi
8 10.1063/1.4804727 , 2013.

9 Várnai, T. and Marshak, A.: Observations of three-dimensional radiative effects that influence
10 MODIS cloud optical thickness retrievals, *J. Atmos. Sci.*, 59, 1607-1618, 2002.

11 Várnai, T. and Marshak, A.: View angle dependence of cloud optical thickness retrieved by
12 MODIS, *J. Geophys. Res.*, 112, D06203, doi:10.1029/2005JD006912, 2007

13 Venema, V., Meyer, S., García, S. G., Kniffka, A., Simmer, C., Crewell, S., Löhnert, U.,
14 Trautmann, T., and Macke A.: Surrogate cloud fields generated with the Iterative Amplitude
15 Adapted Fourier Transform algorithm, *Tellus A*, 58A, 104-120, 2006.

16 Yamaguchi, T., and Feingold, G.: Technical note: Large-eddy simulation of cloudy boundary
17 layer with the Advanced Research WRF model, *JAMES*, 4, doi:10.1029/2012MS000164,
18 2012.

19 Yang, H., Dobbie, S., Mace, G. G., Ross, A., and Quante, M.:GEWEX Cloud System Study
20 (GCSS) cirrus cloud working group: development of an observation-based case study for
21 model evaluation, *Geosci. Model Dev.*, 5, 829-843, 2012.

22

23

24

25

26

27

28

29

1 **Tables**

2

3 Table 1. Time step, process time for one time step and process time for 2h-simulation with
 4 3DCLOUD model, as a function of the numerical resolution. DYCOMS2-RF01 and BOMEX
 5 cases are presented. A comparison between 3DCLOUD and BRAMS LES computation time
 6 for a specific DYCOMS2-RF01 case is added. 3DCLOUD (Matlab code) runs on a personal
 7 computer with Intel Xeon E5520 (2.26 GHz) and BRAMS (Fortran code) runs on a
 8 PowerEdge R720 with Intel Xeon E5-2670 (2.60GHz), both of them having a single-
 9 processor configuration.

Study case	Point mesh $N_x \times N_y \times N_z$	Horizontal numerical resolution Δx [m]	Time step [s]	Process time [s]	Process time for 2h- simulation [s]
DYCOMS2- RF01	$50 \times 50 \times 50$	200	10	0.4	290
	$100 \times 100 \times 50$	100	7	1.3	1340
	$200 \times 200 \times 50$	50	5	5	7200
	$400 \times 400 \times 50$	25	3	18	43200
BOMEX	$50 \times 50 \times 70$	200	30	0.7	170
	$100 \times 100 \times 70$	100	25	2.5	720
	$200 \times 200 \times 70$	50	20	10	3600
	$400 \times 400 \times 70$	25	14	40	20600
DYCOMS2- RF01	$100 \times 100 \times 100$	40	13	2.7	1500
3DCLOUD BRAMS	$100 \times 100 \times 100$	40	0.3	2	48600

10

11

1 **Figure captions**

2

3 Figure 1. General flow chart of the stratocumulus, cumulus and cirrus generator 3DCloud.
4 Note that 3DCloud algorithm is divided in two distinct steps.

5

6 Figure 2. Time series of (a) the mean cloud top height, (b) the mean cloud base height, (c) the
7 cloud coverage, and (d) the liquid water path. The DYCOM2-RF01 case is displayed. The
8 solid lines indicate 3DCLOUD results. The dotted lines indicate a mean over all LES results.
9 The light shading around this mean delimits the maximum and minimum values within the
10 master ensemble at any given time.

11

12 Figure 3. Mean profiles averaged over the fourth hour of (a) the longwave net flux, (b) the
13 liquid water potential temperature, (c) the total water mixing ratio, (d) the liquid water mixing
14 ratio, (e) the horizontal velocity components, and (f) the air density. The DYCOM2-RF01
15 case is displayed. The solid lines indicate 3DCLOUD results. The dotted lines indicate a mean
16 over all LES results. The light shading around this mean delimits by the maximum and
17 minimum values within the master ensemble at any given height.

18

19 Figure 4. Time series of (a) the cloud coverage and (b) the liquid water path. The BOMEX
20 case is displayed. The solid lines indicate 3DCLOUD results. The light shading delimits the
21 maximum and minimum values within the master ensemble at any given time.

22

23 Figure 5. Mean profiles averaged over the fifth hour of (a) cloud coverage, (b) the potential
24 temperature, (c) the water vapour mixing ratio, (d) the liquid water mixing ratio, (e) the
25 horizontal velocity components, and (f) the air density. The BOMEX case is displayed. The
26 solid lines indicate 3DCLOUD results. The light shading delimits the maximum and
27 minimum values within the master ensemble at any given height.

28

29 Figure 6. Time series of vertically-integrated ice water path (IWP) from different cirrus
30 models, which participated in the Idealized Cirrus Model Comparison Project and from the

1 3DCLOUD model (thick blue lines). The upper panel is for the cold cirrus case and the
2 bottom one is for the warm cirrus case. Cyan line represents models with bin microphysics,
3 red line models with bulk microphysics, green line single column models, and thin black lines
4 models with heritage in the study of deep convection or boundary layer clouds. This figure is
5 made from the one taken from Starr et al. (2000) and Yang et al. (2012).

6

7 Figure 7. The instantaneous cloud-field snapshots of the pseudo albedo at four hours
8 simulated by (a) the UCLA-0 model (picture taken from Stevens et al., 2005), (b) the BRAMS
9 model, both configured following the DYCOMS2-RF01 case (Stevens et al., 2005) and (c)
10 from 3DCLOUD with assimilation of meteorological profiles based on the DYCOMS-RF01
11 case. The UCLA-0 field is drawn from simulation where $N_x = N_y = 192$ and $\Delta_x = \Delta_y = 20$
12 m. Both BRAMS and 3DCLOUD are drawn from simulations where $N_x = N_y = N_z = 100$,
13 $\Delta_x = \Delta_y = 40$ m and $\Delta_z = 12$ m. Note that the 3DCLOUD field is obtained at the second step
14 of the algorithm, with the inhomogeneity parameter $\rho_\tau = 0.3$, mean optical depth $\bar{\tau} = 10$ and
15 $L_{out} = 2$ km. (d) is the optical depth power spectra computed following the x and the y
16 directions and then averaged, for BRAMS (points) and 3DCLOUD (circles). A theoretical
17 power spectrum with spectral slope $\beta = -5/3$ is added (black line).

18

19 Figure 8. (a), (b), (c) and (d) pseudo albedo and (e), (f), (g), and (h) cross sections of the
20 vertical velocity (shaded) and the cloud water (contoured), at the end of simulation, for the
21 stratocumulus simulated by 3DCLOUD with assimilation of meteorological profiles based on
22 the DYCOMS2-RF01 case. Different numerical spatial resolutions are presented with
23 $\Delta x = \Delta y$: (a) and (e) $\Delta x = 200$ m, (b) and (f) $\Delta x = 100$ m, (c) and (g) $\Delta x = 50$ m and (d) and
24 (h) $\Delta x = 25$ m. (i), (j), (k) and (l) mean profiles of the potential temperature, the liquid water
25 mixing ratio, the horizontal velocity components, and the vapour water mixing ratio. The
26 solid lines indicate meteorological profiles based on DYCOMS2-RF01 case and assimilated
27 by 3DCLOUD. Points, dotted lines, dashed lines and dash-dot lines indicate 3DCLOUD
28 results at the end of simulation for the different numerical spatial resolution $\Delta x = 200$ m,
29 $\Delta x = 100$ m, $\Delta x = 50$ m and $\Delta x = 25$ m, respectively. Number of iterations is 700.

30

1 Figure 9. Same as Fig. 8, for cumulus cloud simulated by 3DCLOUD with assimilation of
2 meteorological profiles based on the BOMEX case. We let 3DCLOUD iterating until 2h-
3 simulation is done.

4

5 Figure 10. Time series of the mean distance between cloud areas for different horizontal
6 numerical spatial resolutions (colored lines) with a constant vertical numerical spatial
7 resolution ($\Delta z = 38.5$ m) and mean distance averaged over the last-half hour of a 2h
8 simulation as a function of numerical spatial resolution (black line with circles). The cumulus
9 cloud is simulated by 3DCLOUD with assimilation of meteorological profiles based on the
10 BOMEX case. Horizontal extensions are $L_x = L_y = 5$ km and vertical extension is $L_z =$
11 2700 m.

12

13 Figure 11. Same as Fig. 8c ($\Delta x = 50$ m), for different assimilated values of the cloud
14 coverage: (a) and (e) $C = 99\%$, (b) and (f) $C = 80\%$, (c) and (g) $C = 50\%$ and (d) and (h)
15 $C = 20\%$.

16

17 Figure 12. (a) Pseudo albedo estimated from optical depth (initial field) simulated in the step
18 1 by 3DCLOUD for the DYCOMS2-RF01 case (see Fig. 8c), (b), (c) and (d) pseudo albedo
19 adjusted in the step 2 of 3DCLOUD for different values of the inhomogeneity parameter ρ_τ
20 and of the outer scale L_{out} . (e) mean power spectra of optical depth along x and y directions.
21 The power spectra are scaled for better visualization. (f) probability density function of
22 optical depth, (g) mean vertical profiles of horizontally averaged optical depth and (h) volume
23 rendering of optical depth for the case 3. ρ_τ and L_{out} are 0.2 and 1 km for case 1, 0.7 and 1 km
24 for case 2 and 0.7 and 10 km for case 3, respectively. Solid lines, dotted lines, dashed lines
25 and dash-dot lines indicate initial field, case 1, case 2 and case 3 fields, respectively.

26

27 Figure 13. Idealized vertical profiles assimilated (dashed lines) and simulated (solid lines) by
28 3DCLOUD during step 1 of (a) the potential temperature and relative humidity and of (b) the
29 horizontal velocity components and the ice water content (IWC), (c) ice water path (IWP)
30 simulated by 3DCLOUD in step 1, (d) IWP simulated by 3DCLOUD in step 2, (e) mean power

1 spectra of IWC along x and y directions after the step 1 and the step 2. (f) IWC probability
2 density functions after step 1 and step 2. (g) IWC volume rendering after step 2. ρ_{IWC} is set
3 to 1 and L_{out} is set to 1 km. Number of iterations is 1000.

4

5 Figure 14. 2D vertical slice of 3DCLOUD ice water content (IWC gm^3) through a 3D
6 simulation at an angle parallel to the wind (a) RC99a case, (b) RC99 case and (c) RC99b case.
7 Fields are obtained from simulations where $N_x = N_y = 200$ and $N_z = 66$ and $\Delta_x = \Delta_y = 250$
8 m and $\Delta_z = 120$ m. Horizontal extensions are $L_x = L_y = 50$ km and vertical extension is
9 $L_z = 8$ km between 4 km and 12 km. Note that the 3DCLOUD fields are smooth because
10 obtained at the first step of the algorithm.

11

12 Figure 15. Same as Fig. 14b but after the second step of the algorithm, where 1D spectral
13 slope is close to $-5/3$ from outer scale $L_{out} = 15$ km to the numerical scale $\Delta x = 250$ m. (a)
14 mean of 3D IWC is $\overline{\text{IWC}} = 0.07 \text{ gm}^{-3}$ and inhomogeneity parameter $\rho_{IWC} = 0.4$ for cloudy
15 voxels. (b) same as (a) but with inhomogeneity parameter ρ_{IWC} , function of height and
16 derived from the 27 December 1999 RADAR measurements between 10 and 12 UTC crudely
17 estimated from the Fig. 2c in Hogan and Kew (2005).

18

19 Figure 16. Vertical profiles for the RC99 case of (a) cloud fraction, (b) mean of $\ln(\text{IWC})$ for
20 the cloudy voxels and (c) standard deviation of $\ln(\text{IWC})$ for cloudy voxels computed from
21 two 3DCLOUD fields obtained at the second step of the algorithm. The solid lines indicate
22 simulation where inhomogeneity parameter is $\rho_{IWC} = 0.4$ and the dotted lines indicate
23 simulation where the parameter ρ_{IWC} , function of height, is derived from the 27 December
24 1999 RADAR measurements between 10 and 12 UTC and crudely estimated from the Fig 2c
25 in Hogan and Kew (2005).

26

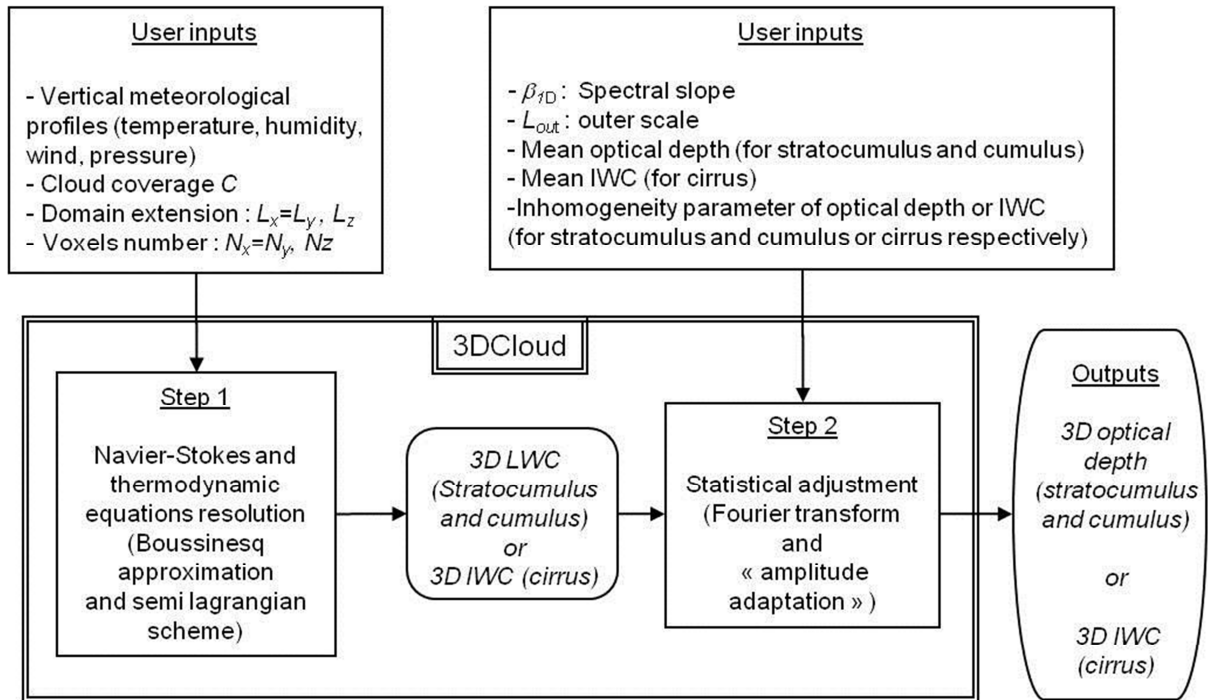
27

28

29

1 **Figures**

2



3

4

5 Figure 1. General flow chart of the stratocumulus, cumulus and cirrus generator 3DCloud.

6 Note that 3DCloud algorithm is divided in two distinct steps.

7

8

9

10

11

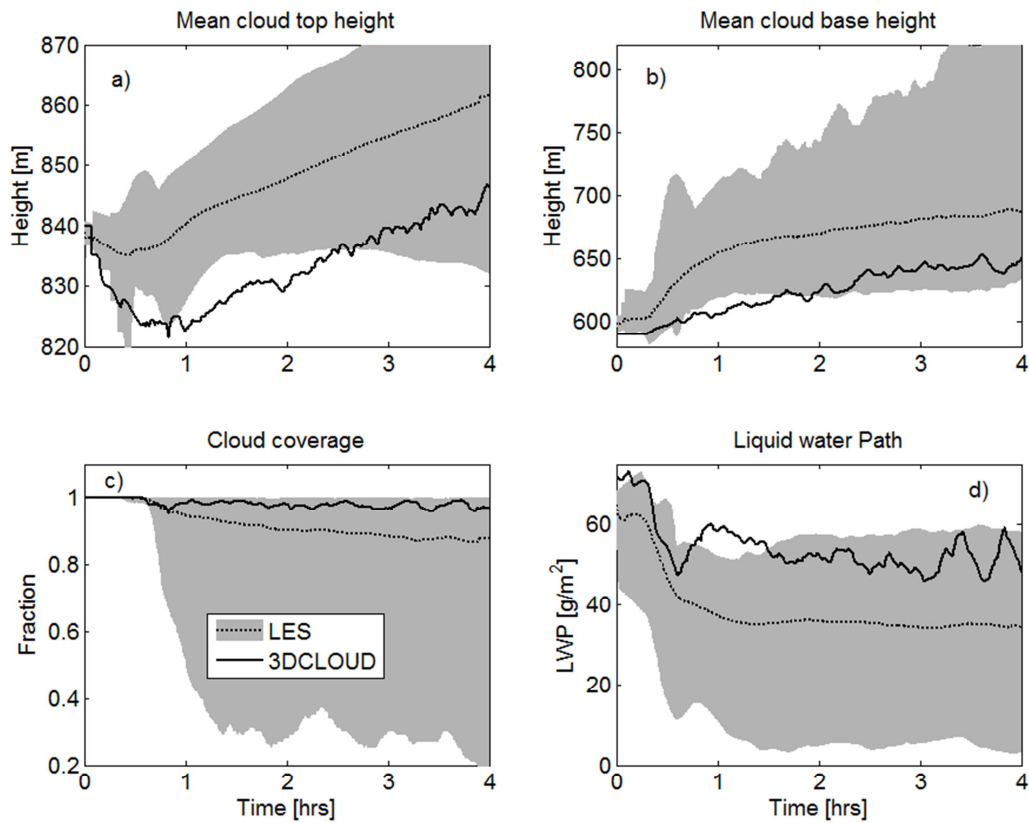
12

13

14

15

16



1

2 Figure 2. Time series of (a) the mean cloud top height, (b) the mean cloud base height, (c) the
 3 cloud coverage, and (d) the liquid water path. The DYCOM2-RF01 case is displayed. The
 4 solid lines indicate 3DCLOUD results. The dotted lines indicate a mean over all LES results.
 5 The light shading around this mean delimits the maximum and minimum values within the
 6 master ensemble at any given time.

7

8

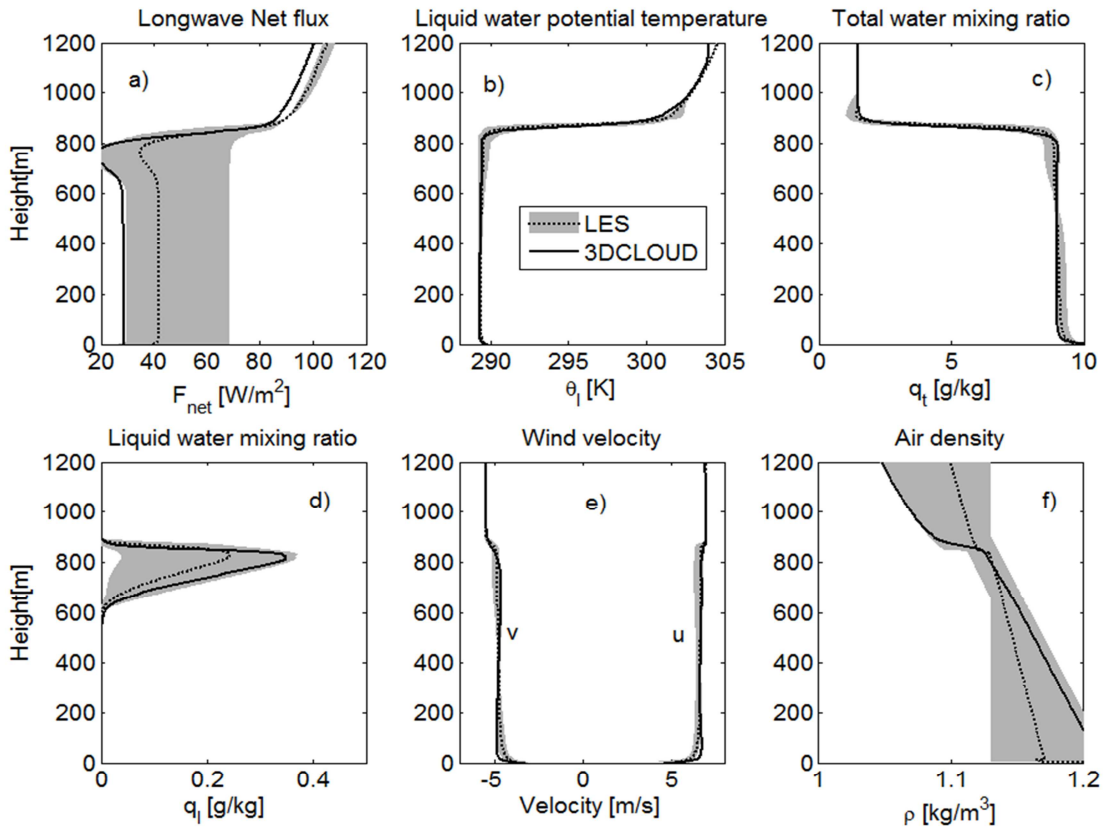
9

10

11

12

13



1

2 Figure 3. Mean profiles averaged over the fourth hour of (a) the longwave net flux, (b) the
 3 liquid water potential temperature, (c) the total water mixing ratio, (d) the liquid water mixing
 4 ratio, (e) the horizontal velocity components, and (f) the air density. The DYCOM2-RF01
 5 case is displayed. The solid lines indicate 3DCLOUD results. The dotted lines indicate a mean
 6 over all LES results. The light shading around this mean delimits by the maximum and
 7 minimum values within the master ensemble at any given height.

8

9

10

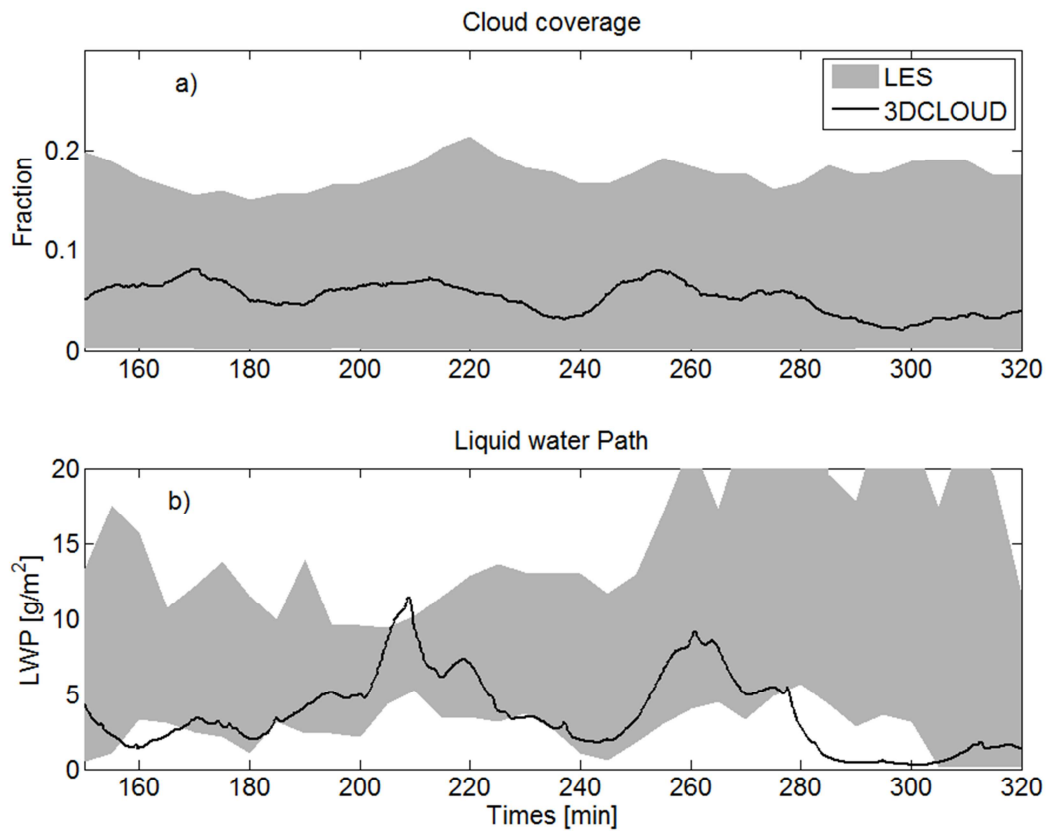
11

12

13

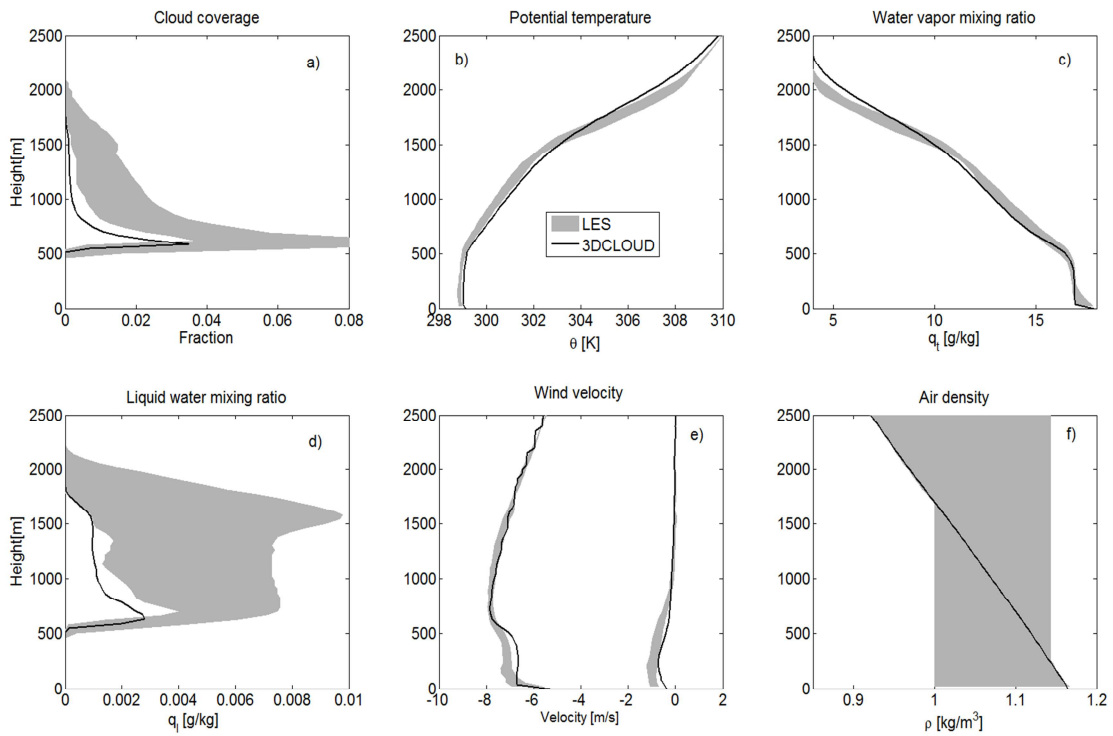
14

15



1
2
3
4
5
6
7
8
9
10
11
12
13
14

Figure 4. Time series of (a) the cloud coverage and (b) the liquid water path. The BOMEX case is displayed. The solid lines indicate 3DCLOUD results. The light shading delimits the maximum and minimum values within the master ensemble at any given time.



1

2 Figure 5. Mean profiles averaged over the fifth hour of (a) cloud coverage, (b) the potential
 3 temperature, (c) the water vapour mixing ratio, (d) the liquid water mixing ratio, (e) the
 4 horizontal velocity components, and (f) the air density. The BOMEX case is displayed. The
 5 solid lines indicate 3DCLOUD results. The light shading delimits the maximum and
 6 minimum values within the master ensemble at any given height.

7

8

9

10

11

12

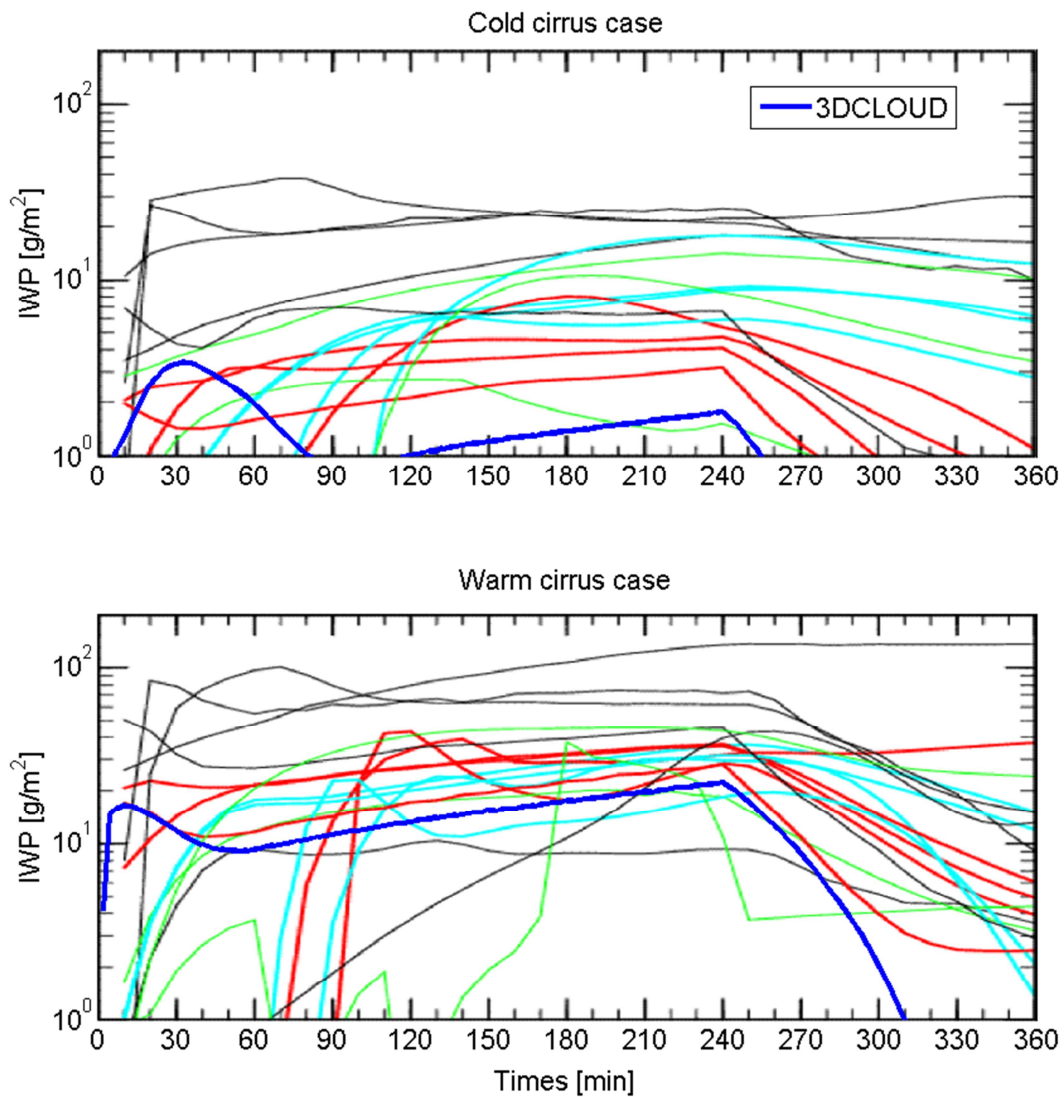
13

14

15

16

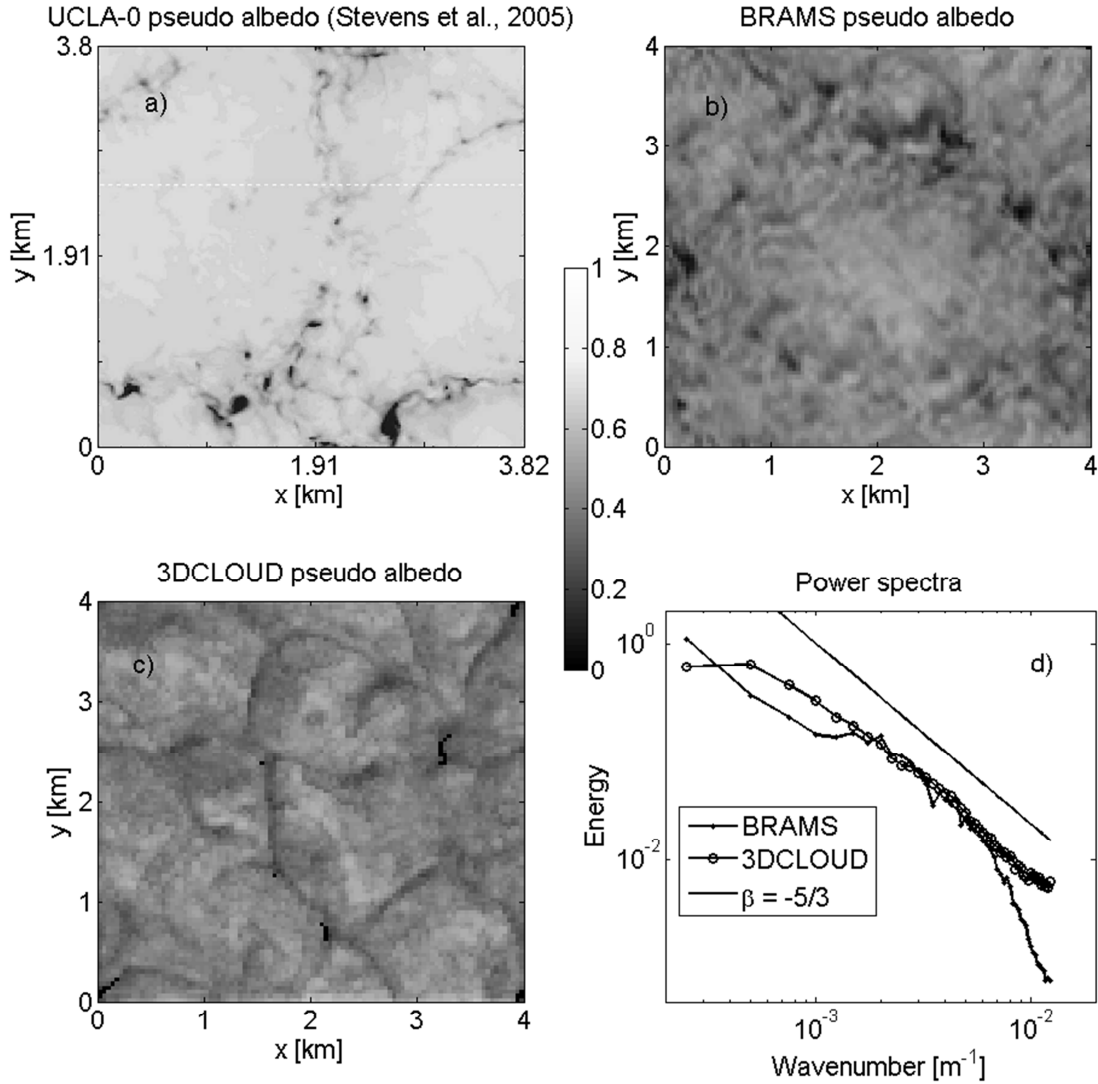
1
2



3

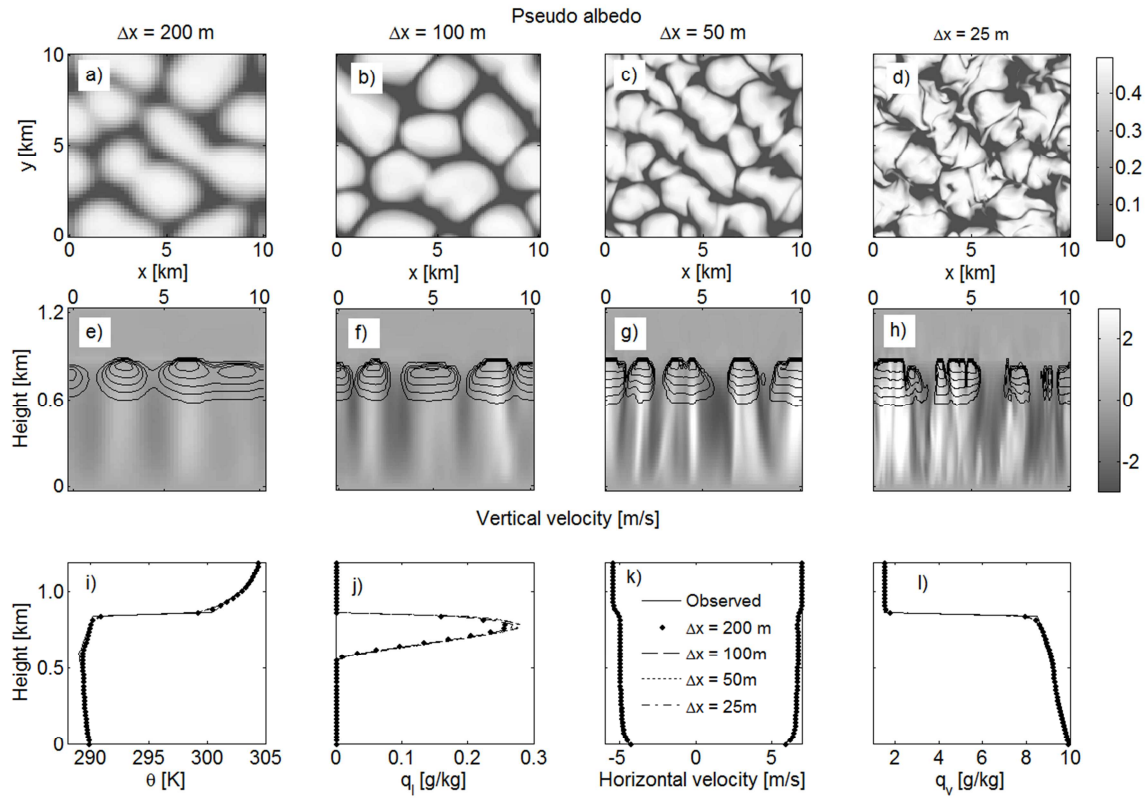
4 Figure 6. Time series of vertically-integrated ice water path (IWP) from different cirrus
5 models, which participated in the Idealized Cirrus Model Comparison Project and from the
6 3DCLOUD model (thick blue lines). The upper panel is for the cold cirrus case and the
7 bottom one is for the warm cirrus case. Cyan line represents models with bin microphysics,
8 red line models with bulk microphysics, green line single column models, and thin black lines
9 models with heritage in the study of deep convection or boundary layer clouds. This figure is
10 made from the one taken from Starr et al. (2000) and Yang et al. (2012).

11



1

2 Figure 7. The instantaneous cloud-field snapshots of the pseudo albedo at four hours
 3 simulated by (a) the UCLA-0 model (picture taken from Stevens et al., 2005), (b) the BRAMS
 4 model, both configured following the DYCOMS2-RF01 case (Stevens et al., 2005) and (c)
 5 from 3DCLOUD with assimilation of meteorological profiles based on the DYCOMS-RF01
 6 case. The UCLA-0 field is drawn from simulation where $N_x = N_y = 192$ and $\Delta_x = \Delta_y = 20$
 7 m. Both BRAMS and 3DCLOUD are drawn from simulations where $N_x = N_y = N_z = 100$,
 8 $\Delta_x = \Delta_y = 40$ m and $\Delta_z = 12$ m. Note that the 3DCLOUD field is obtained at the second step
 9 of the algorithm, with the inhomogeneity parameter $\rho_\tau = 0.3$, mean optical depth $\bar{\tau} = 10$ and
 10 $L_{out} = 2$ km. (d) is the optical depth power spectra computed following the x and the y
 11 directions and then averaged, for BRAMS (points) and 3DCLOUD (circles). A theoretical
 12 power spectrum with spectral slope $\beta = -5/3$ is added (black line).



1

2 Figure 8. (a), (b), (c) and (d) pseudo albedo and (e), (f), (g), and (h) cross sections of the
 3 vertical velocity (shaded) and the cloud water (contoured), at the end of simulation, for the
 4 stratocumulus simulated by 3DCLOUD with assimilation of meteorological profiles based on
 5 the DYCOMS2-RF01 case. Different numerical spatial resolutions are presented with
 6 $\Delta x = \Delta y$: (a) and (e) $\Delta x = 200$ m, (b) and (f) $\Delta x = 100$ m, (c) and (g) $\Delta x = 50$ m and (d) and
 7 (h) $\Delta x = 25$ m. (i), (j), (k) and (l) mean profiles of the potential temperature, the liquid water
 8 mixing ratio, the horizontal velocity components, and the vapour water mixing ratio. The
 9 solid lines indicate meteorological profiles based on DYCOMS2-RF01 case and assimilated
 10 by 3DCLOUD. Points, dotted lines, dashed lines and dash-dot lines indicate 3DCLOUD
 11 results at the end of simulation for the different numerical spatial resolution $\Delta x = 200$ m,
 12 $\Delta x = 100$ m, $\Delta x = 50$ m and $\Delta x = 25$ m, respectively. Number of iterations is 700.

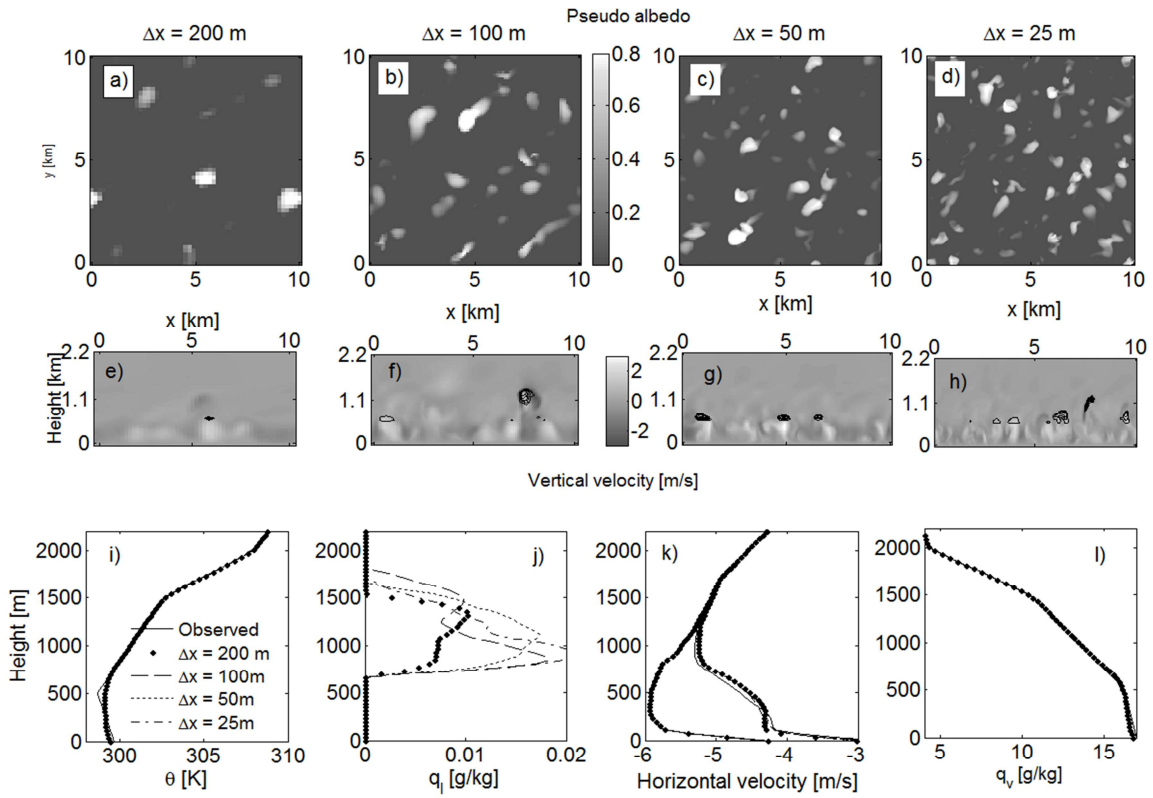
13

14

15

16

17



1

2 Figure 9. Same as Fig. 8, for cumulus cloud simulated by 3DCLOUD with assimilation of
 3 meteorological profiles based on the BOMEX case. We let 3DCLOUD iterating until 2h-
 4 simulation is done.

5

6

7

8

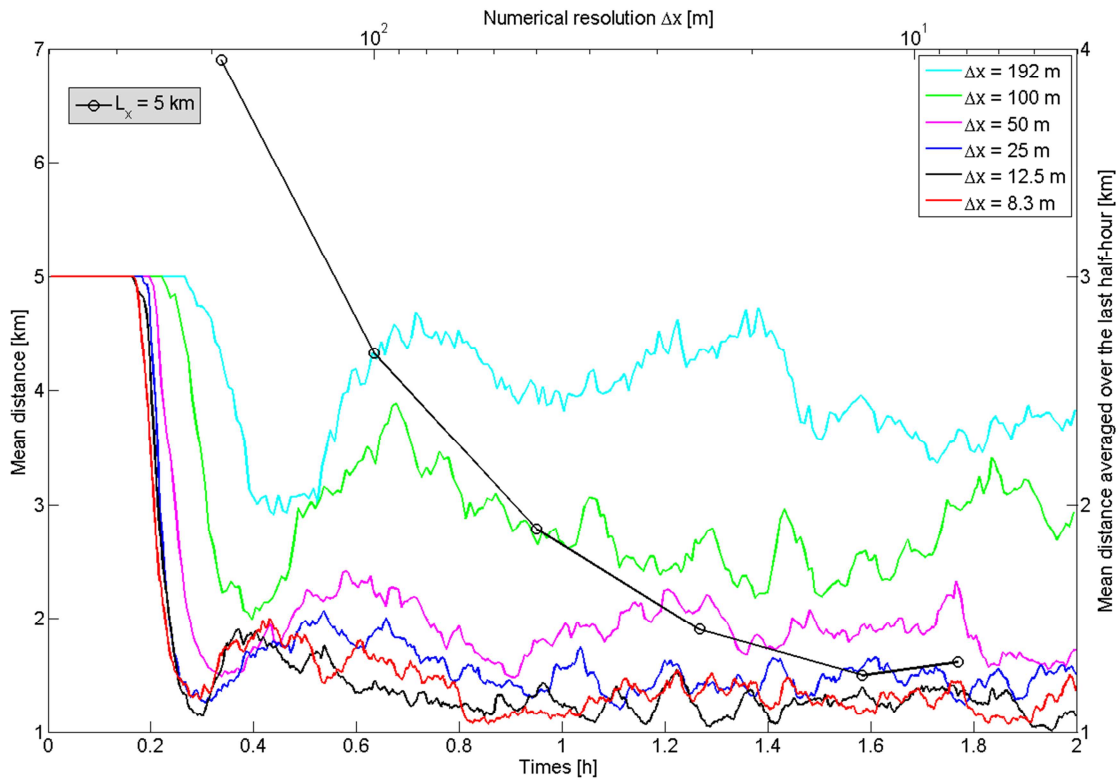
9

10

11

12

13



1

2 Figure 10. Time series of the mean distance between cloud areas for different horizontal
 3 numerical spatial resolutions (colored lines) with a constant vertical numerical spatial
 4 resolution ($\Delta z = 38.5$ m) and mean distance averaged over the last-half hour of a 2h
 5 simulation as a function of numerical spatial resolution (black line with circles). The cumulus
 6 cloud is simulated by 3DCLOUD with assimilation of meteorological profiles based on the
 7 BOMEX case. Horizontal extensions are $L_x = L_y = 5$ km and vertical extension is $L_z =$
 8 2700 m.

9

10

11

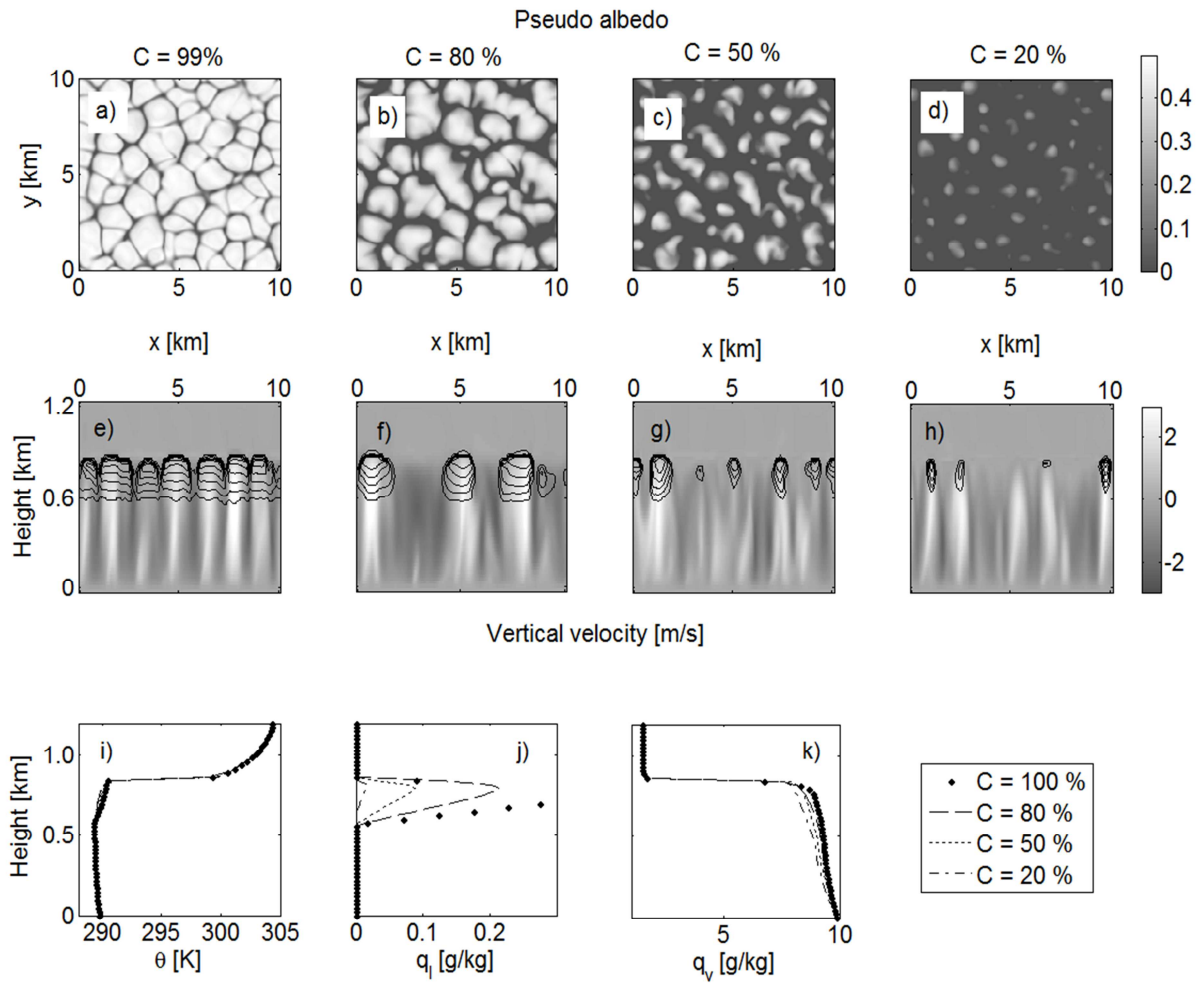
12

13

14

15

16



1

2 Figure 11. Same as Fig. 8c ($\Delta x = 50$ m), for different assimilated values of the cloud
 3 coverage: (a) and (e) $C = 99\%$, (b) and (f) $C = 80\%$, (c) and (g) $C = 50\%$ and (d) and (h)
 4 $C = 20\%$.

5

6

7

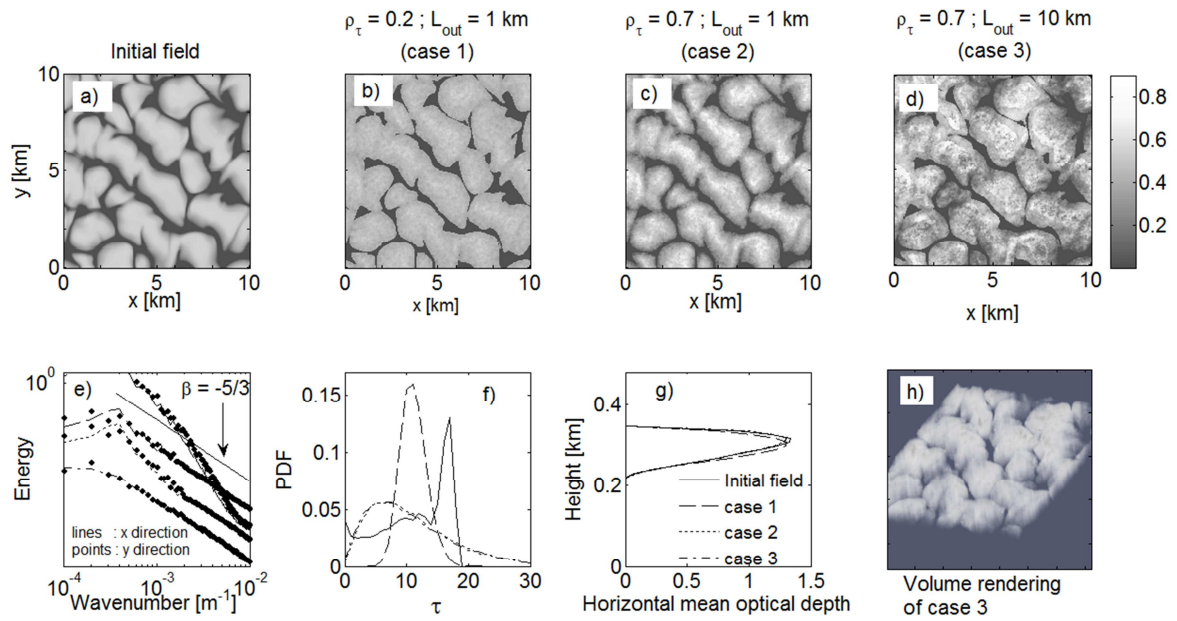
8

9

10

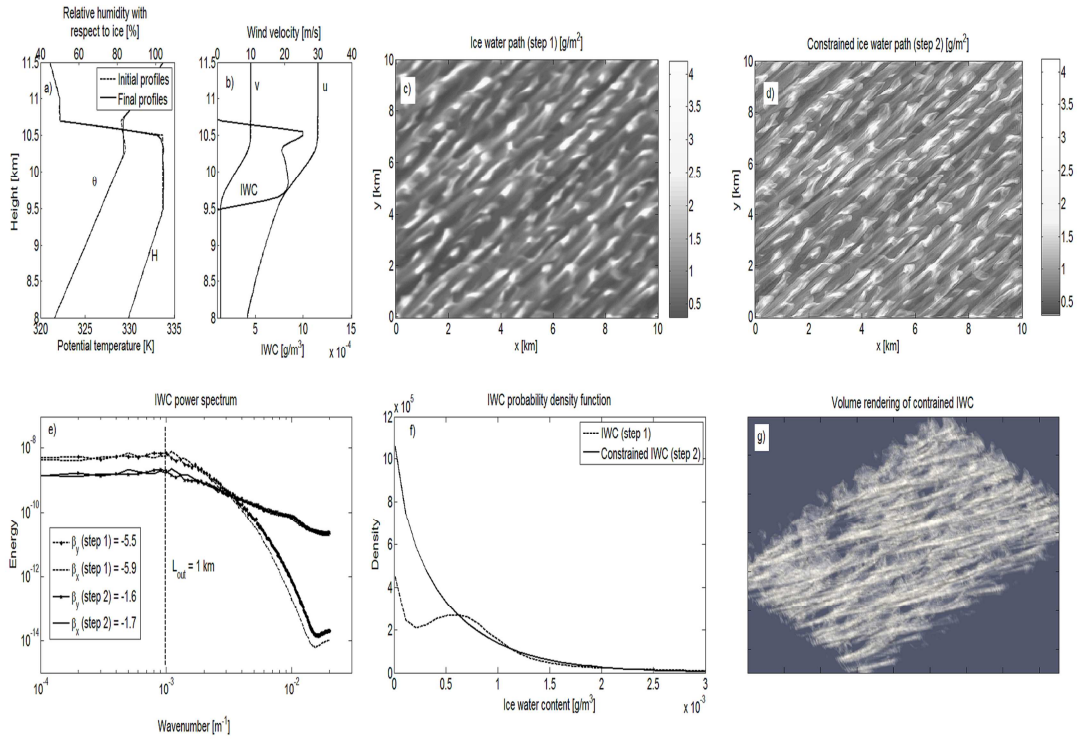
11

12



1
2 Figure 12. (a) Pseudo albedo estimated from optical depth (initial field) simulated in the step
3 1 by 3DCLOUD for the DYCOMS2-RF01 case (see Fig. 8c), (b), (c) and (d) pseudo albedo
4 adjusted in the step 2 of 3DCLOUD for different values of the inhomogeneity parameter ρ_τ
5 and of the outer scale L_{out} . (e) mean power spectra of optical depth along x and y directions.
6 The power spectra are scaled for better visualization. (f) probability density function of
7 optical depth, (g) mean vertical profiles of horizontally averaged optical depth and (h) volume
8 rendering of optical depth for the case 3. ρ_τ and L_{out} are 0.2 and 1 km for case 1, 0.7 and 1 km
9 for case 2 and 0.7 and 10 km for case 3, respectively. Solid lines, dotted lines, dashed lines
10 and dash-dot lines indicate initial field, case 1, case 2 and case 3 fields, respectively.

11
12
13
14
15
16
17
18
19



1

2 Figure 13. Idealized vertical profiles assimilated (dashed lines) and simulated (solid lines) by
 3 3DCLOUD during step 1 of (a) the potential temperature and relative humidity and of (b) the
 4 horizontal velocity components and the ice water content (IWC), (c) ice water path (IWP)
 5 simulated by 3DCLOUD in step 1, (d) IWP simulated by 3DCLOUD in step 2, (e) mean power
 6 spectra of IWC along x and y directions after the step 1 and the step 2. (f) IWC probability
 7 density functions after step 1 and step 2. (g) IWC volume rendering after step 2. ρ_{IWC} is set
 8 to 1 and L_{out} is set to 1 km. Number of iterations is 1000.

9

10

11

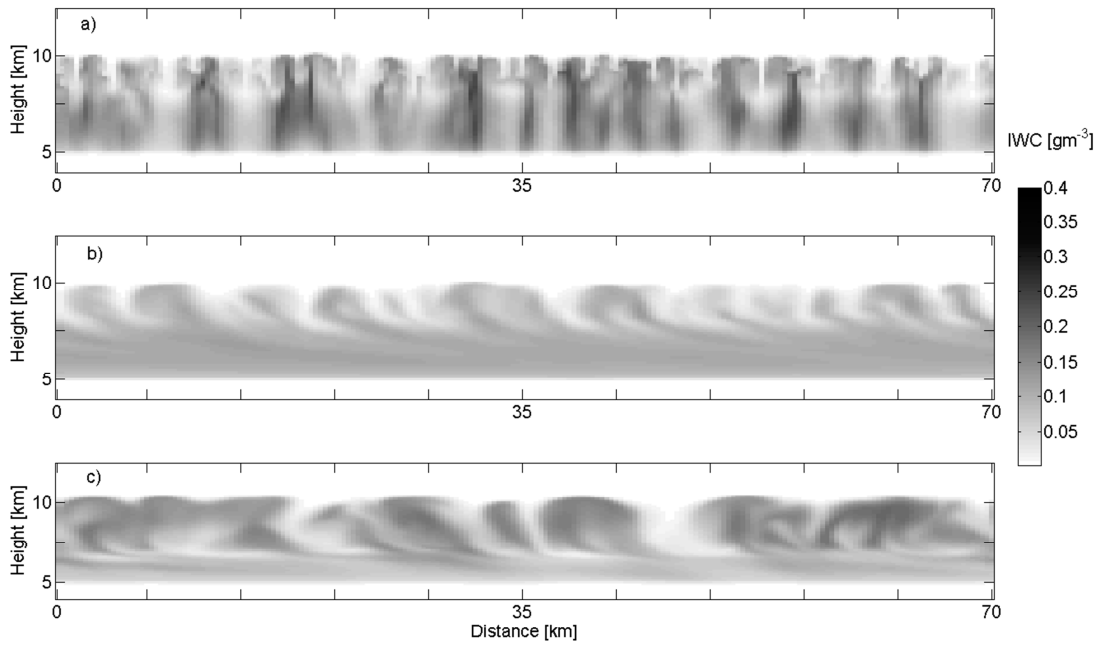
12

13

14

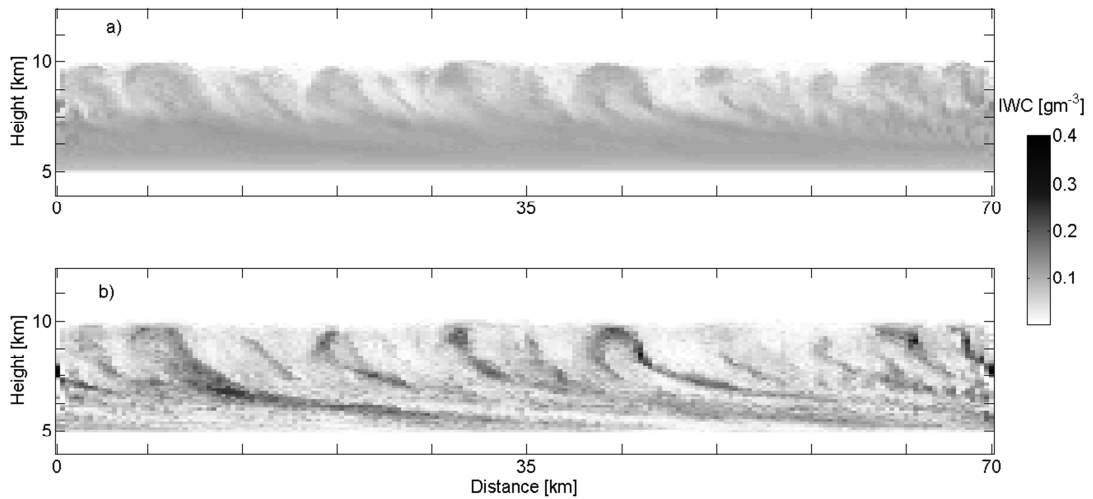
15

16



1
 2 Figure 14. 2D vertical slice of 3DCLOUD ice water content (IWC gm^3) through a 3D
 3 simulation at an angle parallel to the wind (a) RC99a case, (b) RC99 case and (c) RC99b case.
 4 Fields are obtained from simulations where $N_x = N_y = 200$ and $N_z = 66$ and $\Delta_x = \Delta_y = 250$
 5 m and $\Delta_z = 120$ m. Horizontal extensions are $L_x = L_y = 50$ km and vertical extension is
 6 $L_z = 8$ km between 4 km and 12 km. Note that the 3DCLOUD fields are smooth because
 7 obtained at the first step of the algorithm.

8
 9
 10
 11
 12
 13
 14
 15
 16
 17



1

2 Figure 15. Same as Fig. 14b but after the second step of the algorithm, where 1D spectral
 3 slope is close to $-5/3$ from outer scale $L_{out} = 15$ km to the numerical scale $\Delta x = 250$ m. (a)
 4 mean of 3D IWC is $\overline{IWC} = 0.07 \text{ gm}^{-3}$ and inhomogeneity parameter $\rho_{IWC} = 0.4$ for cloudy
 5 voxels. (b) same as (a) but with inhomogeneity parameter ρ_{IWC} , function of height and
 6 derived from the 27 December 1999 RADAR measurements between 10 and 12 UTC crudely
 7 estimated from the Fig. 2c in Hogan and Kew (2005).

8

9

10

11

12

13

14

15

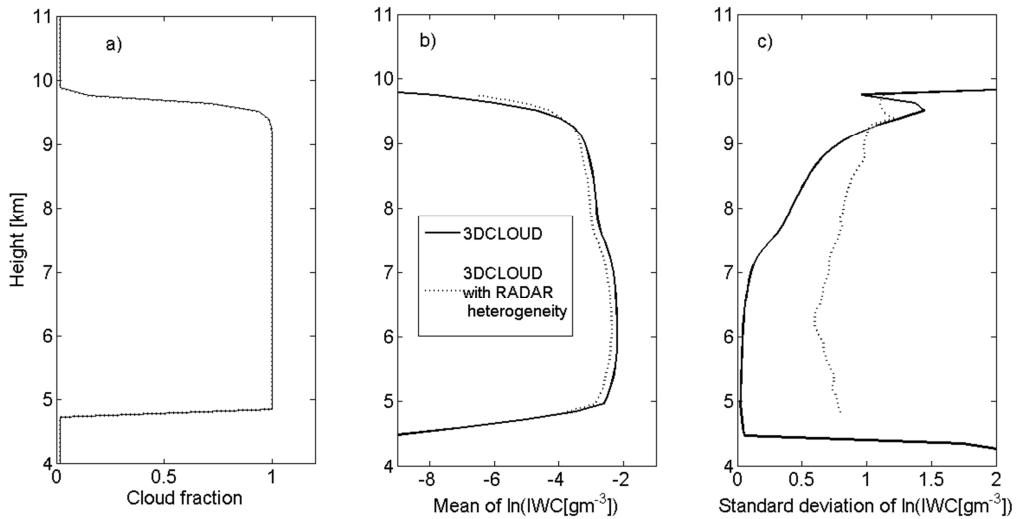
16

17

18

19

20



1

2 Figure 16. Vertical profiles for the RC99 case of (a) cloud fraction, (b) mean of $\ln(\text{IWC})$ for
 3 the cloudy voxels and (c) standard deviation of $\ln(\text{IWC})$ for cloudy voxels computed from
 4 two 3DCLOUD fields obtained at the second step of the algorithm. The solid lines indicate
 5 simulation where inhomogeneity parameter is $\rho_{\text{IWC}} = 0.4$ and the dotted lines indicate
 6 simulation where the parameter ρ_{IWC} , function of height, is derived from the 27 December
 7 1999 RADAR measurements between 10 and 12 UTC and crudely estimated from the Fig 2c
 8 in Hogan and Kew (2005).

9

10

11

12